Journal of Energy Storage 140 (2025) 118998

Contents lists available at ScienceDirect

Journal of Energy Storage

journal homepage: www.elsevier.com/locate/est

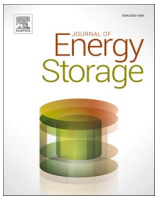

Research Papers

Cryogenic hydrogen storage on peanut shell-derived-activated carbons: Isotherm, kinetics and mechanism

Yasemin Turhan *, Merve Boyluca Yeşilbiçer, Berna Koçer Kizilduman, Mehmet Doğan, Zeynep Bicil

Balikesir University, Faculty of Science and Literature, Department of Chemistry, 10145 Çağış, Balıkesir, Turkey

ARTICLE INFO

Keywords:
Peanut shell
Hydrothermal processing
Activated carbon
Hydrogen storage
Isotherm
Kinetics

ABSTRACT

This study investigates the cryogenic hydrogen storage performance of activated carbons synthesized from peanut shells via hydrothermal carbonization. Samples were prepared at 240 °C for 1, 3, and 6 h using $ZnCl_2$ as the activating agent. Comprehensive characterization was conducted using BET, FTIR-ATR, XRD, SEM/EDX and TGA devices. The PS-$ZnCl_2$-240-3 h sample exhibited the highest BET surface area (856 m^2/g) and total pore volume (0.448 cm^3/g), achieving a maximum hydrogen uptake of 2.1 wt% at 77 K and 30 bar. Adsorption behavior was analyzed using Langmuir, Freundlich, Dual-Langmuir, and Temkin isotherm models. The best fit was obtained with the Langmuir model ($R^2 > 0.996$), indicating monolayer physisorption. Kinetic data were fitted to pseudo-first-order and pseudo-second-order models; the latter showed superior correlation, particularly for the 3 h sample ($R^2 = 0.9874$). Boyd and Weber–Morris models revealed that intraparticle diffusion was the rate-limiting step. Comparative analysis confirmed that the 3 h activation condition yielded the most favorable combination of surface area, microporosity, and hydrogen storage capacity. These results demonstrate that peanut shell-derived activated carbons are promising, low-cost candidates for hydrogen storage applications under cryogenic conditions, offering competitive performance based on surface and pore structure optimization.

1. Introduction

Hydrogen energy, particularly green hydrogen, plays a critical role in the global transition to renewable energy systems. As an environmentally friendly alternative to fossil fuels, hydrogen has the potential to significantly reduce greenhouse gas emissions [1]. It serves as a long-term energy storage solution compatible with the intermittent nature of renewable energy sources, enhances grid stability, and facilitates the decarbonization of hard-to-abate sectors [2]. Many countries have incorporated hydrogen into their energy transition strategies and have promoted its use through updated energy policies. Although hydrogen has a high gravimetric energy density—approximately three times greater than gasoline—and produces zero greenhouse gas emissions upon oxidation, safe and efficient storage remains one of the key challenges. The U.S. Department of Energy has set a gravimetric target of 5.5 wt% reversible hydrogen storage for automotive applications, and achieving this target depends on the development of cost-effective and high-performance materials [3,4]. However, current market and technological limitations have necessitated the reevaluation of these targets, leading to a growing demand for materials capable of higher hydrogen uptake [5]. The interaction of hydrogen with solid materials is generally categorized into two mechanisms: physisorption and chemisorption. In physisorption, molecular hydrogen interacts with the adsorbent through weak Van der Waals forces, electrostatic interactions, and orbital overlap. However, due to its nonpolar nature and low polarizability, hydrogen molecules exhibit weak interactions with the surface, limiting adsorption capacity [6,7]. Therefore, hydrogen storage via physisorption is typically favored at cryogenic temperatures (77 K). Compared to conventional storage methods like compressed gas or liquid hydrogen, solid-state adsorbents offer advantages such as enhanced volumetric density, greater safety, and improved efficiency [8].

Among the various solid adsorbents studied for hydrogen storage, materials such as metal-organic frameworks (MOFs), zeolites, polymers, clays, and amine-functionalized porous materials have attracted attention. However, carbon-based materials stand out due to their exceptional thermal stability, chemical resistance, recyclability, low cost, and wide availability [9,10]. Hydrogen storage in these materials primarily

* Corresponding author.
E-mail address: yozdemir@balikesir.edu.tr (Y. Turhan).

https://doi.org/10.1016/j.est.2025.118998
Received 8 May 2025; Received in revised form 29 August 2025; Accepted 15 October 2025
Available online 21 October 2025

occurs through physisorption, diffusion, and Kubas-type interactions, making high-surface-area carbon-based materials and transition metal-doped nanocomposites highly promising candidates [11]. Carbonaceous materials such as activated carbon, carbon nanotubes, graphene, carbon sphere and their derivatives offer large surface areas and tunable porosity, which enable effective hydrogen uptake [12–16]. Hydrogen adsorption on porous activated carbons presents significant advantages over other methods, including rapid adsorption/desorption kinetics, no energy input requirement for hydrogen release, and high adsorption at low temperatures and moderate pressures. As a result, carbon materials with high porosity are considered primary candidates to meet the gravimetric hydrogen storage targets [17–19].

Activated carbon is one of the most widely used adsorbents in industry due to its high surface area, suitable pore structure, high carbon content, and excellent physicochemical stability. It is widely employed in air and water purification systems, as a catalyst or catalyst support, and in electrochemical applications [20–23]. However, commercial production often relies on expensive carbon-rich precursors with low inorganic content [24,25]. In recent years, to reduce production costs, agricultural wastes [26,27], by-products [28,29] and other biomass sources [30] have been explored as sustainable and low-cost alternatives. Peanut shells, as lignocellulosic waste with high carbon content and low ash yield, are particularly attractive as precursors for activated carbon production. Various studies have focused on the use of agricultural wastes such as peanut shells for the production of activated carbon due to their low cost, sustainability, and environmentally friendly characteristics. Li et al. reported that the carbon material derived from peanut shells and activated with KOH exhibited a high surface area of 3728 m^2/g and a total pore volume of 2.21 cm^3/g, achieving a hydrogen storage capacity of 6.36 wt% at 77 K and 40 bar [31]. Arslanoğlu et al. synthesized activated carbon in a single step using peanut shells and vinasse, obtaining a surface area of 1290.5 m^2/g, and demonstrated high adsorption capacities for dye and heavy metal removal [32]. Zhong et al. produced activated carbon from peanut shells using microwave-assisted phosphoric acid activation and reported favorable surface properties and effectiveness in H_2S removal applications. Sandeep and et al. chosed the peanut shells as a precursor to prepare the cost-effective electrode material for supercapacitors [33]. These studies indicate that activated carbons derived from peanut shells possess significant hydrogen storage potential due to their high surface area and suitable pore structure. In particular, materials obtained through KOH activation have shown notably high hydrogen adsorption capacities [34]. Faraji and Saidi showed the process of biochar production from peanut Shell biomass was investigated experimentally and theoretically and they specified it was favorable for being used as a gas adsorbent [35]. However, to date, no comprehensive study has systematically investigated the hydrogen storage performance of hydrothermally carbonized peanut shell-based activated carbons under cryogenic conditions using detailed kinetic and isothermal modeling. In this context, it is hypothesized that the porous structure and surface chemistry of activated carbons synthesized from peanut shells via one-step hydrothermal carbonization significantly influence their hydrogen adsorption capacity under low temperature and moderate pressure conditions. Therefore, the aim of this study is to develop low-cost, high-surface-area activated carbons from peanut shells via hydrothermal carbonization and evaluate their hydrogen storage behavior at cryogenic temperatures using advanced kinetic and isotherm models. The resulting activated carbons were characterized by Brunauer-Emmett-Teller (BET), Fourier-transform infrared spectroscopy (FTIR-ATR), scanning electron microscopy with energy dispersive X-ray analysis (SEM/EDX), and thermogravimetric/derivative thermal analysis (TGA/d[TG]). Hydrogen storage measurements were conducted using a Hiden IMI-PSI instrument at cryogenic temperatures under various pressures. Moreover, the adsorption kinetics and mechanisms of hydrogen were analyzed using pseudo-first order, pseudo-second order, Elovich, Boyd, and Weber-Morris models, while isothermal behavior was assessed with Freundlich, Langmuir, Dual-Langmuir, and Temkin equations.

2. Experimental

2.1. Materials

The peanut shells used in the experiments were procured from the Yarış village located within the Şamlı district of Balıkesir Province in Turkey. Zinc chloride ($ZnCl_2$) used as the chemical activation agent was purchased from Sigma-Aldrich company. All other chemicals were bought of analytical purity and used within further purification.

2.2. Method

2.2.1. Grinding of peanut shells

Peanut shells were washed with distilled water several times to remove impurities and dried in an oven at 80 °C for 24 h. The dried peanut shells were ground with a laboratory steel mixer using liquid nitrogen and dried again in an oven at 80 °C for 24 h. The dried biomass was sieved on a Retsch AS 200 using 100 μm and 500 μm sieves, and peanut shells with grain sizes of 100–500 μm were obtained.

2.2.2. Preparation of activated carbons

The production of samples was carried out by hydrothermal carbonization method from peanut shells with grain size of 100–500 μm. Samples were prepared using an autoclave system resistant to high pressure and temperature. 50 mL of distilled water and/or reaction solution and 2.5 g of ground peanut shells were placed in the autoclave system and experiments were carried out by mixing at a stirring speed of 500 rpm with help of a closed system magnetic bar. Activated carbons were produced at 240 °C, in $ZnCl_2$ reaction media at a ratio of 1/1 by mass (w/w) and different reaction times (1, 3 and 6 h) and under spontaneous pressure. The samples obtained were washed many times with plenty of distilled water with the help of a vacuum engine, then passed through ethyl alcohol and dried at 80 °C for 6 h.

2.3. Characterization

Peanut shells as a starting material with grain size of 100–500 μm used in the preparation of activated carbons and produced activated carbons were characterized using BET, FTIR-ATR, XRD, SEM/EDX and TGA devices.

BET surface area measurements of carbon-derived materials were carried out with a Quantachrome Nova 2200e series device by degassing at 250 °C for 24 h. Surface area measurements and pore size distributions of the samples were determined by using pure nitrogen gas as an adsorbate under liquid nitrogen at 77 K. In addition, in the pore size distribution of samples, the total pore volume was determined by the DFT method and the micropore volume was determined by the t-plot method using the BET surface area device. FTIR-ATR analyzes of carbon-derived materials were carried out with a Perkin Elmer Spectrum 100 spectrophotometer in transmittance mode in the wave number range of 4000–650 cm^{-1}. XRD analyses of the samples were carried out at room temperature using a Malvern Panalytical Philips X'Pert-Pro diffractometer, operated at 30 mA and 40 kV, over a 2θ range of 5° to 80° with a scanning rate of 2°/min. The surface of activated carbons was coated with Au—Pd under 20 mA current for a certain period of 60 s, and their morphologies were visualized with a Zeiss Evo LS 10 scanning electron microscope. Thermogravimetric analyzes of activated carbons were performed using Perkin Elmer Diamond simultaneous TG analyzer in the temperature range of 30–1200 °C with 20 °C temperature increases under nitrogen atmosphere.

2.4. Hydrogen storage analyzes

Hydrogen adsorption measurements of the activated carbon samples

were conducted using a Hiden IMI-PSI high-pressure gas sorption analyzer equipped with a cylindrical sample cell. The hydrogen gas used in the experiments was of ultra-high purity (>99.999 %) and supplied from a 200 bar high-pressure cylinder. The working pressure range of the analyzer extended from high vacuum up to 100 bar, while the temperature range spanned from cryogenic temperatures to 500 °C. In this study, all measurements were performed at −196 °C (liquid nitrogen temperature). Prior to analysis, the activated carbon samples (typically 50–100 mg) were degassed under vacuum at 200 °C for approximately 8 h to remove any adsorbed impurities. The system was then pressurized with hydrogen to the desired pressure level, and the pressure drop was continuously monitored to evaluate hydrogen uptake. The measurement process was fully automated to ensure high data quality and reproducibility. All necessary precautions were taken to minimize potential sources of error, including gas leakage, temperature fluctuations, and pressure variations due to hydrogen diffusion into the sample cell. These measures ensured accurate and reliable adsorption data [36].

3. Results and discussion

3.1. Characterization

Characterization of the produced activated carbons was carried out using BET, FTIR-ATR, XRD, SEM/EDX and TG/d[TG] techniques.

3.1.1. FTIR-ATR analysis

Fig. 1 shows the FTIR-ATR spectra for peanut shells and activated carbons. The FTIR-ATR spectrum for peanut shells exhibited various bands belonging to different functional groups. This spectrum shows characteristic peaks corresponding to cellulose, hemicellulose, lignin, and various organic compounds. A wide and spreading band around 3336 cm^{-1} corresponds to stress vibrations belonging to the OH hydroxyl group, and the peak at 2921 cm^{-1} is attributed to –CH stress vibrations indicating the presence of methyl and methylene groups (the broad absorption in 3100–2800 cm^{-1} region indicates the presence of aliphatic compounds). The peak at 1734 cm^{-1} is associated with C═O stress vibrations (peaks at 1730 cm^{-1} and 1637 cm^{-1} suggest the presence of carbonyl and aromatic groups, respectively). The peaks in 1604 cm^{-1} and 1507 cm^{-1} correspond to the C═C tensile vibration, while the other bands in 1259 and 1232 cm^{-1} show the bending vibrations of the –CH group. The characteristic peak at 1026 cm^{-1} corresponds to the C—O stress vibrations [37]. The spectrum also reflects the complex composition of peanut shells biomass, highlighting its potential applications in biofuels, agricultural residues, and other sustainable uses. When the FTIR-ATR spectra of activated carbons are compared with the spectrum of peanut shells, it is seen that most of the functional groups in the peanut shells are lost with the formation of activated carbon. This situation is also similar to the spectra of activated carbons obtained from different biomass [38]. In the synthesis of activated carbon with $ZnCl_2$ activation, $ZnCl_2$ promotes pore formation in the carbon skeleton and is then removed by washing. Therefore, peaks directly related to Zn are not expected in the FTIR spectra. The hydroxyl bands expected to be observed at 3500–3000 cm^{-1} in the FTIR spectra of the synthesized activated carbons after activation were not present because the C—H structures were removed during activation. The disappearance of the bands at 1750–1700 cm^{-1} and 1300–1000 cm^{-1} compared to biomass can be attributed to the disintegration of carbonyl, carboxyl, quinone and ester in the biomass structure into gaseous products by C═O and C—O stretches, respectively. The increase in the band at 1600–1500 cm^{-1} in activated carbon samples may be due to C═C aromatic ring vibrations due to the increase in the carbon content of activated carbons [22,39]. In addition, since the hydrothermal carbonization process results in condensation and aromatization, more pronounced C═C peaks are expected.

3.1.2. XRD analysis

The XRD patterns of peanut shells and activated carbons are given in Fig. 2. The characteristic peaks obtained from the XRD pattern of the peanut shells are $2\theta = 22°$ and $2\theta = 72.73°$. The $2\theta = 22°$ peak, which corresponds to the 002 crystallographic plane of the peanut shells cellulose I lattice, belongs to the typical cellulose diffraction peak [40]. The characteristic peaks of the peanut shells are not seen in the XRD patterns of the hydrocarbonized samples treated with $ZnCl_2$. These patterns confirm that the samples have an amorphous structure rather than a crystalline structure [41].

3.1.3. SEM/EDX images

Although a porous structure is observed in the surface image of the peanut shells at 1500× magnification given in Fig. 3a, the surface is relatively smooth [42]. According to the surface morphologies of the samples viewed at different magnification ratios, it can be said that the surface morphology of the peanut shells changes significantly as the hydrothermal carbonization time increases, the pore structure becomes

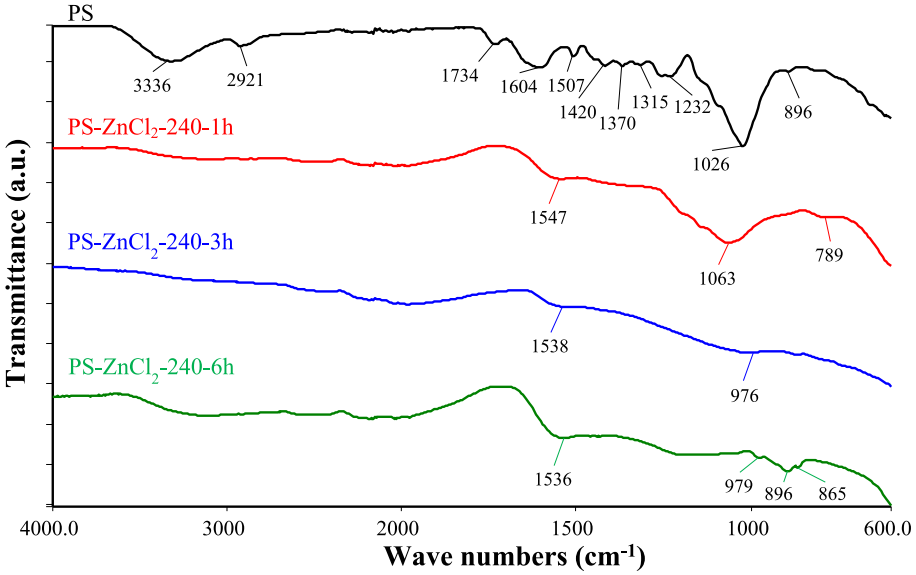

Fig. 1. FTIR-ATR spectra of peanut shells and activated carbons.

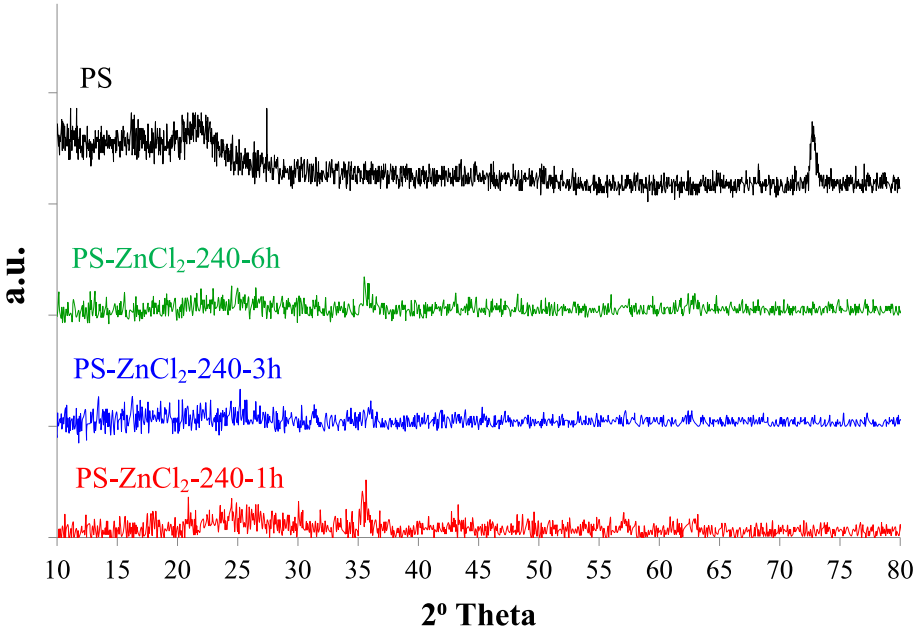

Fig. 2. XRD patterns of peanut shells and activated carbons.

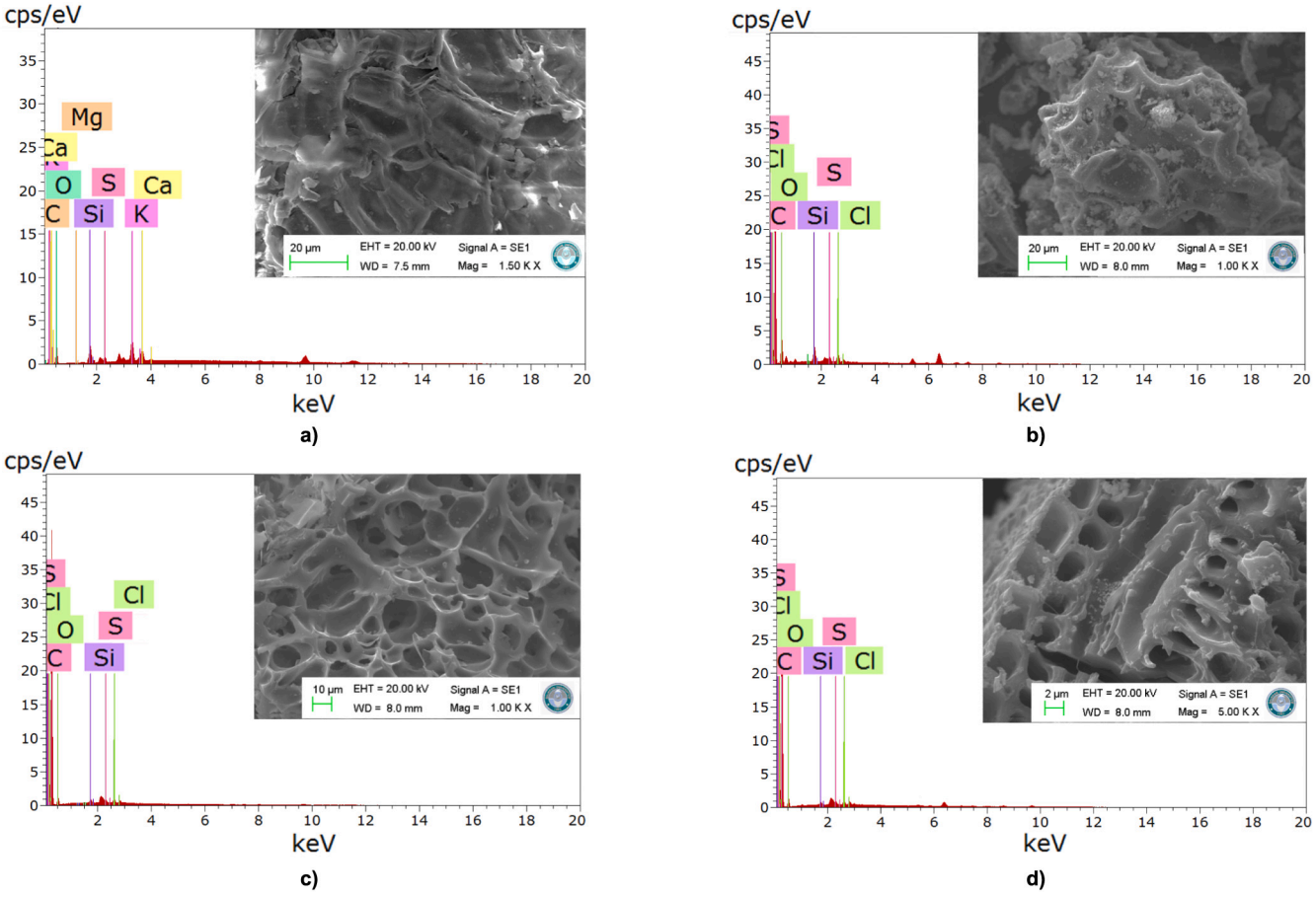

Fig. 3. SEM/EDX images of a) peanut shells, b) PS-$ZnCl_2$-240-1 h, c) PS-$ZnCl_2$-240-3 h, d) PS-$ZnCl_2$-240-6 h activated carbons.

more pronounced and it gains the character of activated carbon. While the surface morphology and pore formation of the activated carbon samples are clearly observed from the SEM images zoomed in at 1000× and 5000×, nothing clear can be said about the micro and mesopore structure [43]. While the peanut shells are relatively smooth and less porous, the porous structure becomes more pronounced in the surface morphology of the sample activated with 1 h hydrothermal carbonization (Fig. 3b), and collapse and fragmentation occur on the surface. In

the SEM images of the samples activated with 3 h and 6 h of hydrothermal carbonization, given in Fig. 3c and d, respectively, it is seen that the pores become more distinct, the pore structure is well developed and approaches more activated carbon character, and this situation is also compatible with the increased surface areas [36,44,45]. In addition, the high magnification ratio (5000×) of the sample synthesized with 6 h of hydrothermal carbonization provides a clearer view of the pores, in this example it is seen that the pore diameters become smaller and the structure becomes more irregular. When evaluated in general, the SEM images of activated carbons show that hydrothermal carbonization promotes pore formation.

EDX analysis is a frequently used method to determine the elemental content of biomasses such as peanut shells and the carbon and oxygen percentage of activated carbons synthesized from biomasses. According to the EDX spectrum given in Fig. 3a, the main components of the peanut shells are 46.95 % carbon (C) and 37.27 % oxygen (O) and these two elements constitute a large part of the total composition. The high carbon content indicates that the lignocellulosic structure and organic content of the peanut shells are dominant. The presence of oxygen is due to oxygen-containing compounds such as cellulose, hemicellulose and lignin in the structure of the biomass. In addition, 7.11 % potassium (K), 3.46 % silicon (Si), 0.98 % sulfur (S), 3.71 % calcium (Ca) and 0.50 % magnesium (Mg) were detected. These elements can generally originate from environmental contamination or minerals taken from the soil during the growth of the peanut and the soil structure in which the plant grows [46,47]. An increase in the amount of carbon and a decrease in the amount of oxygen are expected in the elemental compositions of the activated carbon samples obtained after hydrothermal carbonization because functional groups containing oxygen are removed from the structure by thermal decomposition. Therefore, C and O are the main elements in the EDX spectrum to evaluate the synthesis of activated carbon. When the EDX spectra of the samples activated with 1 h, 3 h and 6 h of hydrothermal carbonization and the % elemental compositions given in Table 1 are evaluated, it is seen that they contain 70.99 % C and 25.45 % O, 88.14 % C and 10.40 % O, 84.75 % C and 13.67 % O, respectively. These results show that hydrothermal carbonization successfully produces activated carbon by improving the pore structure on the surface together with $ZnCl_2$ and enriches the carbon content by removing organic components. The ratios of elements such as Si and S may have changed in the EDX analysis and the source of these trace elements observed in the composition of activated carbons is probably the composition of the raw material. In addition, the presence of Cl in activated carbons is due to the activation of $ZnCl_2$. In addition, after 3 h of carbonization, the carbon content increased to the maximum while the oxygen content decreased. As can be seen from the SEM image, the maximum pore formation was observed in this sample and compared to other samples, the carbon content reached the highest level while the oxygen and inorganic compounds decreased to the lowest level.

3.1.4. Thermal analysis

The TG and d[TG] thermograms of the peanut shells and activated carbons are given in Fig. 4a and b and the data obtained from these thermograms are given in Table 2. TGA was used to determine the moisture content and stability of the biomass and also the thermal stability of activated carbons. It is clear from this thermogram that the degradation mechanism of the peanut shells occurs in 2 steps between room temperature and 1200 °C. In the first step between 30 and 200 °C, a mass loss of 5.75 % occurred. This loss may be due to the moisture released from the sample during heating. TG analysis of peanut shells revealed that the main decomposition occurred in the second step between 200 and 600 °C (T_{max2}: 350 °C), which may be due to the decomposition of chemically bound water, cellulose, hemicelluloses and lignin into carbon [48–50]. The mass loss in this step was 72.5 % and the maximum mass loss occurred at 350 °C. With heating above 400 °C, low weight loss occurs due to the formation of volatile products such as CO, CO_2, etc. [51]. In addition, the amount of residue left from the decomposition at the end of the analysis was 21.8 %. According to Carrier, hemicellulose is the first component of woody biomass to decompose in the internal environment [52]. Hemicellulose begins to decompose at approximately 250 °C to 300 °C. After hemicellulose, cellulose begins to decompose at approximately 300–350 °C. Finally, the decomposition of lignin occurs at 300–500 °C. TG studies provide information about the thermal stability of activated carbons. TG thermograms of activated carbons are given in Fig. 4b. With the hydrothermal carbonization process, the thermal stability of the samples increased compared to the untreated peanut shells. Table 2 shows the increase in T_{max1}, T_{max2}, T_{max3} and T_{max4} temperatures confirming this stability. In addition, when the samples were heated up to 1200 °C under nitrogen environment, there was an increase in the amount of residue compared to the untreated peanut shells. The degradation mechanism of the high surface area activated carbon samples obtained under these conditions occurs in a single step at 941 °C. Only the sample group that decomposed in a single step was the one that was activated with $ZnCl_2$ for 6 h. According to this table, the TG results show that there are significant differences in the residual mass among samples activated for 1 h, 3 h, and 6 h (e.g., residue for the 1 h sample is 59.7 %, for the 3 h sample is 75 %, and for the 6 h sample is 67.5 %). The degradation peaks of the activated carbon samples whose degradation profiles changed after activation shifted to higher temperatures, especially in the 3 h sample. This indicates that the activation process increases the aromatic carbon content of the samples and forms a dense carbon skeleton resistant to high temperatures [53]. While 1 h was deemed insufficient for the activation period, 6 h may have caused pore collapse, a decrease in surface area and micro-mesopore volume. A 3-h activation period may represent the condition where the pore structure developed optimally and the structure reached its most stable form with a high carbon/mineral skeleton ratio. This may also be the main reason why this sample had the maximum hydrogen storage capacity compared to other samples. This finding also demonstrates the importance of controlled optimization in determining the activation period. The use of activating agents such as KOH, $ZnCl_2$, or H_3PO_4 not only increases the porosity of activated carbon but also improves its pore size distribution, ensuring optimal hydrogen adsorption. This process facilitates the formation of distinct micro- and mesoporous architectures, which are crucial for the effective physical adsorption of hydrogen molecules. Therefore, the development and development of chemical activation procedures is essential to optimize the potential of ACs for hydrogen storage [54,55].

Table 1
Elemental composition (wt%) of peanut shells and activated carbons.

Samples	C	O	Si	S	Ca	Mg	K	Cl
PS	46.95	37.27	3.46	0.98	3.71	0.50	7.11	–
PS-$ZnCl_2$-240-1 h	70.99	25.45	1.60	0.65	–	–		1.25
PS-$ZnCl_2$-240-3 h	88.14	10.40	0.34	0.41	–	–		0.58
PS-$ZnCl_2$-240-6 h	84.75	13.67	0.36	0.54	–	–		0.67

3.2. Hydrogen storage

In hydrogen storage, BET surface area and pore volume are the basic parameters that determine the adsorption capacity [56]. High BET surface area increases the number of active points where hydrogen molecules can be retained by physical adsorption. Appropriately sized and high volume pore structure facilitates the effective retention and release of hydrogen. Therefore, these two properties directly affect the storage performance, especially in porous solid adsorbents. In the study, activated carbons were produced from peanut shells by hydrothermal method at 240 °C for 1, 3 and 6 h. The hydrogen storage capacities of the produced activated carbons measured at cryogenic temperature are given in Fig. 5. From the figure, it is seen that the storage capacities for

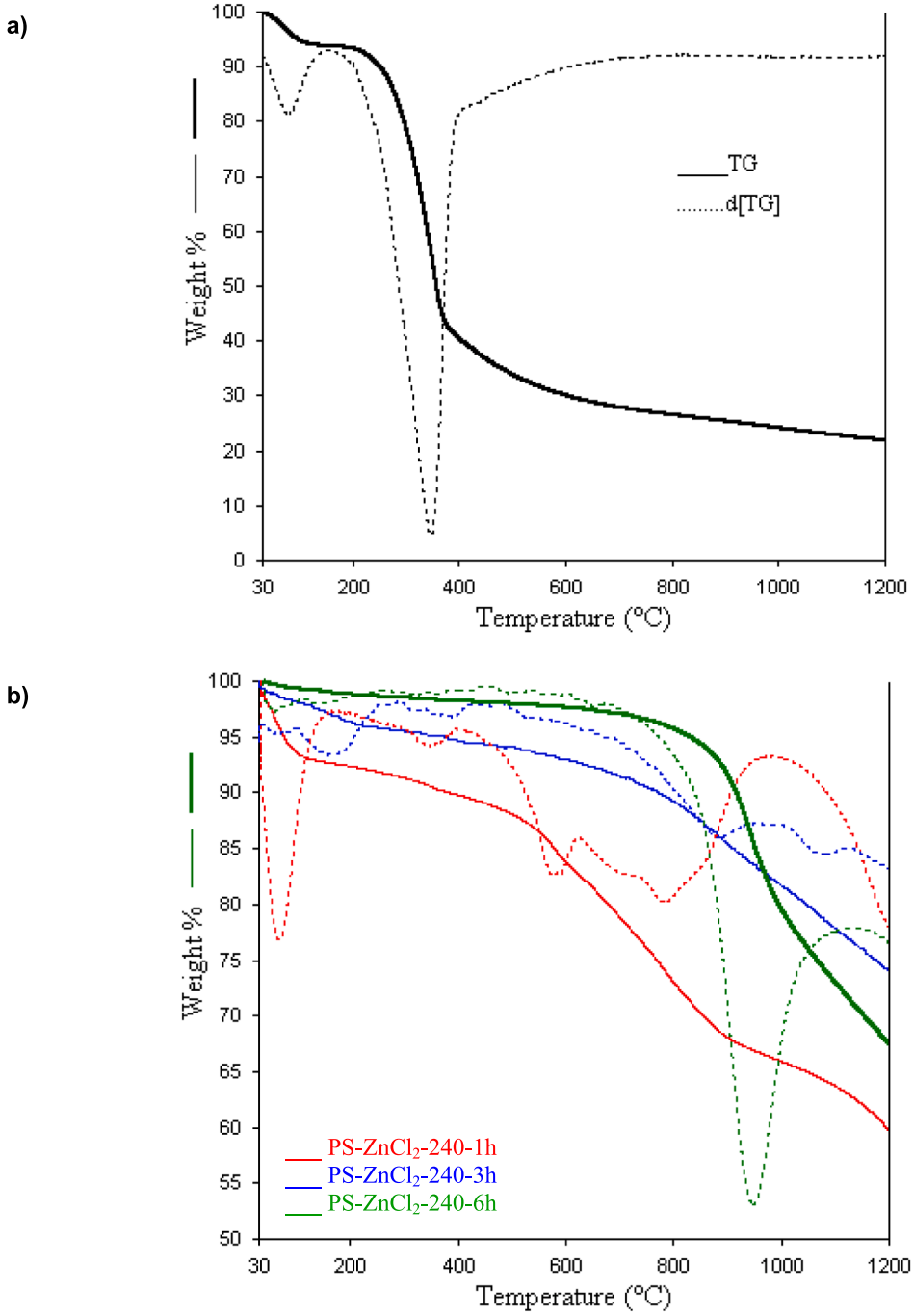

Fig. 4. TG and d[TG] thermograms of a) peanut shells and b) activated carbons.

Table 2
Thermal stability parameters of peanut and activated carbons.

Samples	T_{max1} (°C)	ΔY_1 (%)	T_{max2} (°C)	ΔY_2 (%)	T_{max3} (°C)	ΔY_3 (%)	T_{max4} (°C)	ΔY_4 (%)	Residue (%)
PS	74	5.8	350	72.5	–	–	–	–	21.8
PS-$ZnCl_2$-240-1 h	69	7.5	318.7	2.8	583	12.0	1199	18.0	59.7
PS-$ZnCl_2$-240-3 h	65	2.9	857	12.6	1057	9.5	–	–	75.0
PS-$ZnCl_2$-240-6 h	–	–	–	–	–	–	941	32.5	67.5

all three activated carbon samples increased with increasing pressure, and the storage capacities of other activated carbon samples except the PS-$ZnCl_2$-240-3 h sample tended to decrease slightly after approximately 17.5 bar. This situation shows that PS-$ZnCl_2$-240-1 h and PS-$ZnCl_2$-240-6 h samples exhibit excessive adsorption behavior after a certain pressure. On the contrary, it was determined that the storage capacity of PS-$ZnCl_2$-240-3 h sample increases with increasing pressure. Excessive adsorption is the situation where the gas density in the pore is higher

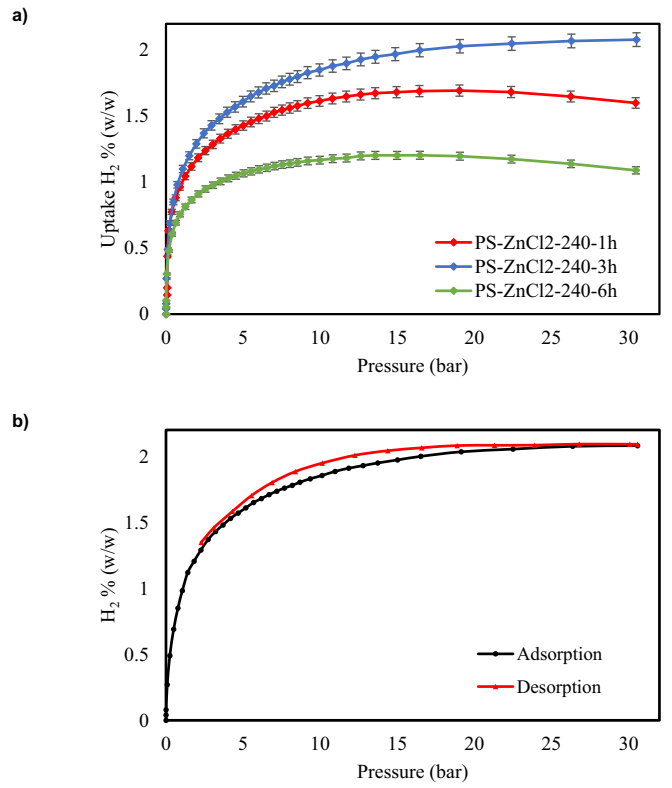

Fig. 5. a) Hydrogen storage capacities of activated carbon samples and b) adsorption/desorption isotherm of PS-$ZnCl_2$-240-3 h.

than the environmental gas density due to the excess adhesion of the gas to the adsorbent surface under certain temperature and pressure conditions. In this case, the adsorption amount of the gas increases with the increase in the number of molecules on the adsorbent surface and the pressure, but after a certain point, the addition of gas decreases due to the repulsion of the existing adsorbed molecules on the surface. The excessive adsorption isotherm curve shows a maximum value as the pressure increases and then decreases as a result of the subsequent pressure increases. This occurs because the gas fills both the adsorbent surface and the internal pores, while the external gas density is still increased. Therefore, excessive adsorption reveals the complexity of the interactions between the gas phase and the solid phase and the effect of the gas density. Similar results have been observed in different studies in the literature. Excessive adsorption was observed during the adsorption of hydrogen on activated carbons synthesized from tangerine peel under low temperature and high pressure. Especially in the measurements made at high pressure at cryogenic temperature (77 K), the isotherms tended to increase to a maximum point and decrease again instead of reaching saturation; this indicates that the hydrogen density in the pores is higher than the surrounding gas. This confirms that excessive adsorption occurs and shows that the adsorption is limited only by physical interactions (van der Waals forces) [57]. In another study, excessive adsorption was observed at a temperature of 77 K and a pressure of approximately 20 bar. Under these conditions, the adsorption capacity reached its maximum due to the filling of the activated carbon pores with hydrogen, and no increase was observed afterwards. In the experiments, activated carbons synthesized using 1:2 and 1:4 $ZnCl_2$ ratios showed the best hydrogen storage performance, especially when pyrolyzed at 600 °C, thanks to their high surface area (2270 m^2/g) and high micropore volume (0.93 cm^3/g). Although the adsorption rate was fast at the beginning as the pressure increased, the adsorption amount was fixed after the pores were filled after 20 bar. This shows that hydrogen was physically adsorbed by van der Waals interactions, especially at low temperatures, and excessive adsorption capacity emerged after the pores were completely filled [38]. In this type of adsorption, especially micropores (<2 nm) are more effective; because the interaction forces between the gas molecules and the surface are more intense in these pores and allow the gas to be trapped in the pores and kept at high density. Therefore, activated carbons with high micropore volume are more advantageous in terms of excessive adsorption capacity. BET analyses were performed to determine the surface areas and pore volumes of the activated carbon samples. Fig. 6 shows the nitrogen adsorption-desorption isotherm curves of the activated carbon samples. According to the IUPAC (International Union of Pure and Applied Chemistry) classification, there are 6 types of isotherm classifications. These classifications are very important for understanding the pore structure and surface properties of the materials [58]. When the nitrogen adsorption-desorption isotherms are examined according to the IUPAC classification, it is seen that all samples have a Type IV isotherm. This isotherm type is particularly characteristic for mesoporous solids and is typically seen with a hysteresis loop [59]. PS-$ZnCl_2$-240-3 h sample exhibits a significant hysteresis loop, indicating that it

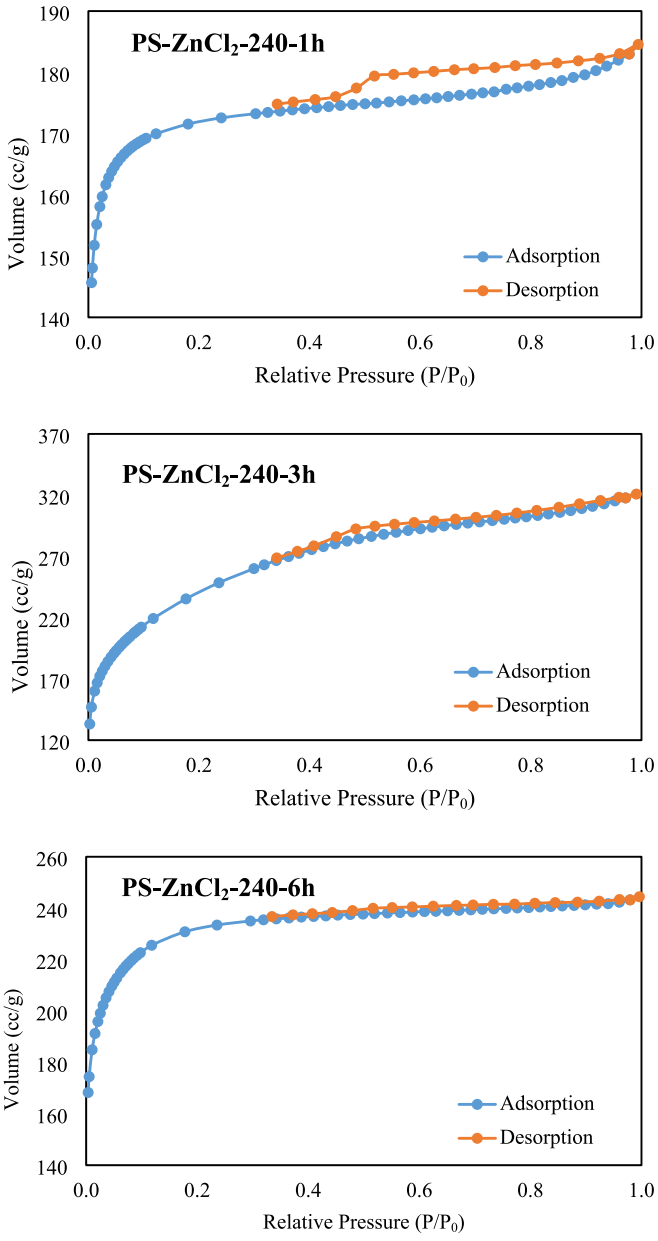

Fig. 6. Nitrogen adsorption-desorption isotherm curves for activated carbon samples.

contains mesoporous structure, while PS-$ZnCl_2$-240-1 h and PS-$ZnCl_2$-240-6 h samples have much more limited hysteresis loop, suggesting that micropores are dominant. In Fig. 7, the pore size distribution and cumulative pore volumes of PS-$ZnCl_2$-240-1 h, PS-$ZnCl_2$-240-3 h and PS-$ZnCl_2$-240-6 h samples are compared. PS-$ZnCl_2$-240-3 h sample has a significant pore density in the range of approximately 1–2 nm and the highest cumulative pore volume around 0.5 cm^3/g. This shows that 3 h of activation supports the formation of both micropores and mesopores. PS-$ZnCl_2$-240-1 h and PS-$ZnCl_2$-240-6 h samples exhibit lower total pore volume and their pore distributions are narrower and they have predominantly microporous structure. Especially PS-$ZnCl_2$-240-1 h sample presents a very limited pore volume, while PS-$ZnCl_2$-240-6 h sample shows lower performance compared to PS-$ZnCl_2$-240-3 h sample despite being more developed in terms of pore volume. This situation reveals that 3 h activation time with $ZnCl_2$ is the most suitable time for optimum pore development. The pore volume values of the samples calculated according to the DFT method are presented in Table 3. The pore volume values calculated according to the DFT method confirm the above results. With the DFT method, the total pore and micropore volumes of PS-$ZnCl_2$-240-1 h, PS-$ZnCl_2$-240-3 h and PS-$ZnCl_2$-240-6 h samples were calculated as 0.250, 0.448 and 0.335 cm^3/g; and 0.250, 0.346 and 0.333 cm^3/g, respectively. In terms of mesopore volume (V_{meso}), the most significant difference is noted as 0.102 cm^3/g in PS-$ZnCl_2$-240-3 h sample, which shows that the formation of mesoporous structures occurs most efficiently in this period. In line with these data, it can be said that 3 h of activation provides the optimum condition in terms of both higher surface area and developed pore structure. According to the IUPAC classification, the hysteresis loop is Type 4, which indicates the presence of slit-type micropores together with mesopores. Therefore, 3 h activation with $ZnCl_2$ provided balanced formation of both micro and mesopores. When Table 3 is examined, it is shown that PS-$ZnCl_2$-240-1 h and PS-$ZnCl_2$-240-6 h samples have quite low mesopore volumes. The fact that microporous structures are more dominant in excessive adsorption is in good agreement with the pore structures of PS-$ZnCl_2$-240-1 h and PS-$ZnCl_2$-240-6 h samples. PS-$ZnCl_2$-240-6 h sample has both micro and mesopore volumes. The fact that excessive adsorption is not observed in this sample may be due to the storage of hydrogen gas in mesopores in addition to micropores with increasing pressure and higher pore volumes.

When Fig. 5a is examined, it is seen that the hydrogen storage capacities of the activated carbon samples are different from each other. It is seen that the differences in hydrogen storage capacities between the samples are related to the presence of BET surface area, micropore volume and mesopore. PS-$ZnCl_2$-240-3 h sample has the highest BET surface area with 856 m^2/g, micropore volume of 0.346 cm^3/g and also a significant mesopore volume (0.102 cm^3/g). Thanks to these properties, it reached the highest hydrogen storage capacity by providing both high surface area and easier diffusion paths for hydrogen molecules. PS-$ZnCl_2$-240-1 h sample showed a more limited adsorption performance with 693 m^2/g surface area and low micropore volume (0.250 cm^3/g). Although the PS-$ZnCl_2$-240-6 h sample was similar to the 1 h sample in terms of surface area (722 m^2/g) and micropore volume (0.333 cm^3/g), it was observed that the long activation time negatively affected the pore structure and decreased hydrogen adsorption. As a result, high BET surface area, large micropore volume and the presence of an appropriate amount of mesopores are critical factors in increasing the hydrogen storage capacity. Especially in the PS-$ZnCl_2$-240-3 h sample, a superior hydrogen adsorption performance was obtained due to the synergistic effect of both the large surface area and the well-balanced micro and mesopore structure.

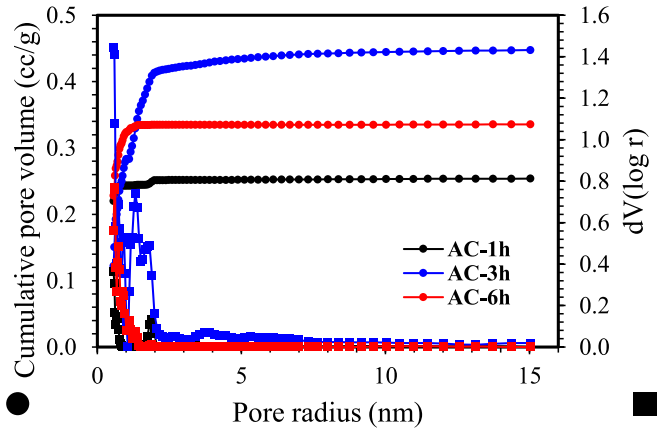

Fig. 7. Variation of cumulative pore volume with pore size for activated carbon samples.

Table 3
BET surface areas and pore size distributions of activated carbons.

Samples	S_{BET}[a] (m^2/g)	V_t[b] (cm^3/g)	V_{DFT}[c] (cm^3/g)	V_{mic}[d] (cm^3/g)	V_{meso}[e] (cm^3/g)
PS-$ZnCl_2$-240-1 h	693	0.285	0.253	0.250	0.003
PS-$ZnCl_2$-240-3 h	856	0.496	0.448	0.346	0.102
PS-$ZnCl_2$-240-6 h	722	0.378	0.335	0.333	0.002

[a] S_{BET}, computed by BET equivalent at P/P^0 = 0.05–0.3.
[b] Vt, predicted from the the amount of N_2 adsorption at P/P^0 = 0.99.
[c] VDFT, measured by DFT method using slit pore model.
[d] Vmic, determined by DR method.
[e] It was achieved by deducting the micropore volume from the pore volume which was analyzed by the DFT technique.

Furthermore, when the adsorption/desorption curve of the PS-$ZnCl_2$-240-3 h sample is examined in Fig. 5b, the desorption isotherm does not overlap with the adsorption isotherm. In this case, the adsorption-desorption isotherm curve exhibits hysteresis. This situation is generally observed in adsorbents that also have mesopores, and when Table 4 is examined, it is seen that this sample has micro- and mesopores [81].

In the literature, the hydrogen storage capacities of activated carbons produced from various biomass and organic sources vary widely depending on temperature, pressure, and the pore characteristics of the

Table 4
Hydrogen storage capacities of some activated carbons.

References	Source	T (K)	Pressures (bar)	H_2 (wt%)
Sethi and Sayari [4]	Petroleum pitch	77	1	2.94
Stock et al. [26]	Orange peel	77	1	2.60–2.80
Stock et al. [26]	Tea leaves	77	1	2.50–2.60
Peng et al. [27]	Bagasse	–*	1	2.62
Peng et al. [27]	Cornstalk	–*	1	2.61
Peng et al. [27]	Pine powder	–*	1	2.13
Selvaraj et al. [28]	Bamboo-chopsticks	77	1	2.30
Stock et al. [29]	Coffee waste	77	37	5.79
Serafin et al. [30]	*Polypodium vulgare* leaves	298	45	2.73
Ariharan and Viswanathan [36]	Peanut shell	298	100	1.20
Türkyilmaz et al. [38]	Horse chestnut shell	77	30	4.46
Doğan et al. [57]	Tangerine peel	77	30	1.67
Doğan et al. [60]	Olive leaf	77	80	0.43
Choi and Park [61]	Biomass derived aerogels	77	1	2.70
Casa-Lillo et al. [62]	Activated carbon fibers	298	10	1
Bicil and Doğan [63]	Almond shell	77	30	2.53
Heo and Park [64]	Rice husk	77	1	2.50
Arshad et al. [65]	Empty fruit bunch	77	20	2.14
Işınkaralar et al. [66]	Horse chestnut shell	77	45	2.2
In this study	Peanut shell	77	30	2.10

* The study temperature is not clear.

material. Adsorption studies conducted at low temperatures (77 K) generally provide higher capacities compared to those carried out at higher temperatures (298 K). This is attributed to the more effective physical adsorption of hydrogen molecules at lower temperatures. Increasing the pressure generally improves the storage capacity; however, beyond a certain point, the increase becomes limited. At 298 K, Casa-Lillo et al. reported a hydrogen storage capacity of 1.00 % for activated carbon fibers at 10 bar [62]. Ariharan and Viswanathan obtained 1.20 % for peanut shell–derived activated carbon at 100 bar [36]. Serafin et al. achieved 2.73 % for activated carbons produced from *Polypodium vulgare* leaves at 45 bar [30]. At 77 K under moderate pressure conditions, Türkyılmaz et al. achieved 4.46 % for activated carbons from horse chestnut shell at 30 bar [38]. Doğan et al. reported 1.67 % for tangerine peel–derived activated carbons under the same conditions [57]. Activated carbons from almond shells reached 2.53 % at 30 bar in the study by Bicil and Doğan [63]. In the present study, peanut shell–derived activated carbon achieved a hydrogen storage capacity of 2.10 % at 77 K and 30 bar. Under low pressure (1 bar) and 77 K conditions, Sethi and Sayari (2016) reported 2.94 % for petroleum pitch–derived activated carbons, while Choi and Park obtained 2.70 % for biomass-derived aerogels [4,61]. Stock et al. achieved 2.60–2.80 % for activated carbons derived from orange peel and 2.50–2.60 % for those from tea leaves [26]. Selvaraj et al. reported 2.30 % for bamboo-chopstick-derived activated carbons [28]. Heo and Park obtained 2.50 % for rice husk-based activated carbons [64]. Peng et al. reported 2.62 % for bagasse, 2.61 % for cornstalk, and 2.13 % for pine powder-derived activated carbons [27]. At 77 K under medium-to-high pressure conditions, Arshad et al. reported 2.14 % for empty fruit bunch–derived activated carbon at 20 bar [65]. Işınkaralar et al. achieved 2.20 % for horse chestnut shell–derived activated carbon at 45 bar [66]. Stock et al. reported 5.79 % for coffee waste–derived activated carbons at 37 bar [29]. In contrast, Doğan et al. obtained only 0.43 % for olive leaf-derived activated carbon at 80 bar [60]. The hydrogen storage capacity of 2.10 % achieved in this study under 77 K and 30 bar is competitive when compared to many results reported in the literature under similar conditions. It falls within the same pressure range as 2.20 % for horse chestnut shell [66] and 2.53 % for almond shell [63], while exceeding the 1.67 % reported for tangerine peel [57]. In conclusion, when the hydrogen storage performances of activated carbons produced from different sources are compared, the value obtained in this study is significant both for its performance under moderate pressure conditions and for the use of a sustainable feedstock such as peanut shell.

Table 5 presents the storage capacity, cost performance, and advantages/disadvantages of the activated carbons obtained in this study and the state-of-the-art technology storage materials. As summarized in Table 5, the peanut shell-derived activated carbon developed in this work shows hydrogen uptake comparable to or better than commercial activated carbons. While its gravimetric and volumetric capacities are lower than those of advanced MOFs and metal hydrides, our material offers remarkable advantages in terms of sustainability, cost-effectiveness, and large-scale availability, since it is obtained from agricultural waste. When benchmarked against the DOE 2025 targets (≥5.5 wt% and ≥40 g/L), the material still requires improvement; however, its favorable cost-to-performance ratio and renewable origin make it a promising candidate for low-cost, practical hydrogen storage applications.

3.3. Isotherm analysis

Isotherm analysis is critical in understanding the adsorption process of gases, determining and optimizing the distribution of gas molecules and its maximum adsorption capacity on the adsorbent surface. In addition, isotherm analysis also elucidates the nature of the adsorption mechanism (physical or chemical) and the surface properties of the adsorbent. The selection of the appropriate isotherm model can generally be optimized by regression coefficient analysis methods, which provides a more accurate description of the adsorption process [74–76]. The isotherms commonly used to analyze the adsorption data of gases are Freundlich, Langmuir, Dual-Langmuir and Temkin isotherms [65].

The Freundlich isotherm is a model based on the energy distribution of active sites on the adsorbent surface for adsorption. This isotherm is an empirical equation that states that at low concentrations the amount of adsorption increases with the adsorbate concentration or pressure and can be written in linear form as follows [77]:

$$\ln q_e = \ln k_F + 1/n \ln P \tag{1}$$

In this equation, q_e is the amount of substance adsorbed (mmol/g); k_F and n are the Freundlich constants; and P is the pressure (bar). If the experimental data are consistent with the Freundlich isotherm, the plot of $\ln q_e$ against lnP should give a straight line with slope 1/n and extrapolation to $\ln k_F$.

The Langmuir isotherm is an equation that models the adsorption of gases on a solid surface and assumes that each adsorption site on the surface can be occupied by only one gas molecule. This model predicts that gas molecules will adsorb to the surface up to a certain maximum saturation level and that there is no interaction between the molecules during this process. The Langmuir isotherm can be given in linear form as follows [63]:

$$\frac{P}{q_e} = \frac{1}{K_1 q_{m1}} + \frac{P}{q_{m1}} \tag{2}$$

Here, q_e is the amount of hydrogen adsorbed (mmol/g); P is the hydrogen pressure (bar); q_{m1} is the monolayer capacity (mmol/g); and K_1 is the equilibrium constant. From the slope and extrapolation of the plot of P/q_e against P, q_{m1} and K_1 can be calculated.

The dual Langmuir model is a powerful tool for relating multicomponent gas adsorption and provides flexibility in describing mixed gas competition while maintaining thermodynamic consistency [78]. In this

Table 5
Comparative performance of hydrogen storage materials.

Material	H_2 storage capacity (wt%)	Operating pressure/ temperature	Approx. cost	Advantages	Disadvantages
Commercial activated carbon [67,68]	0.6–1.8	30–100 bar/77 K	Low–medium	Widely available, inexpensive, stable	Relatively low capacity
MOF-5 [69]	4.5	1–10 bar/77 K	High	Extremely high surface area	Moisture sensitive, expensive
HKUST-1 (Cu-BTC) [70]	2.27–3.6	1–10 bar/77 K	High	Good uptake, well studied	Moisture instability
MIL-101(Cr) [71]	5.6–6.1	1–10 bar/77 K	High	Very high surface area, large pores	High synthesis cost
$LaNi_5H_6$ (metal hydride) [72]	1.0–1.3	<10 bar/room temp.	Medium–high	High volumetric capacity, stable	Heavy, low wt%, kinetic barriers
MgH_2 [73]	6.4–8.8	>300 °C	Low	High gravimetric capacity	Requires high temperature activation
DOE target (2025)	≥5.5	100 bar/40–85 °C	–	Benchmark for applications	Challenging to meet
In this study (peanut shell-derived activated carbon)	2.10	30 bar/77 K	Very low (agricultural waste-based)	Renewable, low-cost, scalable, waste valorization	Moderate wt%, less ordered pore structure

model, each hydrogen molecule is assumed to dissociate and occupy two points. The dual-Langmuir equation can be given as

$$\frac{P^{1/2}}{q_e} = \frac{1}{K_2 q_{m2}} + \frac{P^{1/2}}{q_{m2}} \quad (3)$$

q_{m2} and K_2 in this equation are different numerical values from those in Eq. 2.

Temkin isotherm is a model that describes the adsorption equilibrium conditions by considering the interactions of adsorbent molecules on the surface and surface heterogeneity. This isotherm expresses the relationship between the adsorption pressure (P) and the adsorbed amount in a logarithmic manner at a given temperature. Temkin isotherm is generally valid at low and medium pressures and can be written as the following linear equation [79]:

$$q_e = A\ln P + B \quad (4)$$

In this equation, A and B are specific constants related to the Temkin model.

The regression coefficient was used to determine which isotherm the experimental data are compatible with. The linear regression coefficients calculated by applying the experimental data to the Freundlich, Langmuir, Dual-Langmuir and Temkin isotherms are given in Table 6. It is seen that the regression coefficients for the Freundlich isotherm vary in the range of 0.8421–0.9272; for the Langmuir isotherm, in the range of 0.9964–0.9981; for the Dual Langmuir isotherm, in the range of 0.7876–0.9481; and for the Tamkin isotherm, in the range of 0.9662–0.9954. The highest regression coefficients were obtained for the Langmuir isotherm. Another parameter showing the agreement of the experimental data with the Langmuir isotherm is the agreement of the maximum amount of hydrogen adsorbed at equilibrium with the monolayer capacities calculated for the Langmuir model. This result shows that hydrogen molecules are adsorbed at the active points on the surfaces and pores of the activated carbon samples, there is no interaction between the molecules, the adsorption is limited to the monolayer, and the active points on the activated carbon surface have the same affinity for the hydrogen molecule. In the literature, it has been found that the adsorption of hydrogen on the surface of activated carbons produced from almond shells by chemical and microwave activation is well correlated with the Freundlich isotherm [63]. In another study, the adsorption of hydrogen on the Pt surface was found to be more compatible with the Langmuir model. This is because the Langmuir model is based on the assumption that the adsorbate binds singly to specific binding sites on the surface [80].

3.4. Adsorption rate and kinetics

The kinetics of gas adsorption on adsorbent surfaces is very important for determining the interaction of gas molecules with adsorbent surfaces and the rate-determining step. Adsorption rate expresses how fast molecules adhere to an adsorbent surface. This rate varies depending on the material and environmental conditions and includes molecular transition processes from the gas or liquid phase to the solid phase. Fig. 8 shows the change in hydrogen storage capacities of porous activated carbon samples produced by hydrothermal method at constant $ZnCl_2$ concentration for different periods of time. It is seen that the adsorption rate is quite fast at the beginning and decreases with time. The high rate at the beginning is due to the low coverage fraction of the activated carbon surface and the decrease in the number of active points where gas molecules can interact due to the increase in coverage fraction over time. Again, it is seen from the curves that the hydrogen storage capacities of the samples increase with increasing pressure.

The investigation of adsorption rates as a function of pressure or the amount of adsorbed gas allows the determination of the degree of adsorption. Pseudo-first and second-order kinetic equations are widely used to investigate the adsorption kinetics of adsorbates from the gas or

Table 6
Isotherm constants for adsorption of hydrogen on the activated carbons.

Samples	Langmuir				Dual Langmuir	Freundlich			Temkin		
	$q_{(exp)}$ (mmol)	q_m (mmol)	K_1	R^2	R^2	n	k_F	R^2	A	B	R^2
PS-$ZnCl_2$-240-1 h	0.745 (±0.016)	0.772 (±0.017)	1.166 (±0.025)	0.9978 (±0.0217)	0.7876 (±0.0171)	3.017 (±0.065)	0.351 (±0.008)	0.8421 (±0.0183)	0.116 (±0.003)	0.436 (±0.009)	0.9860 (±0.0214)
PS-$ZnCl_2$-240-3 h	1.343 (±0.033)	1.369 (±0.034)	0.889 (±0.022)	0.9964 (±0.0247)	0.9232 (±0.0229)	2.633 (±0.065)	0.526 (±0.013)	0.9272 (±0.0230)	0.161 (±0.004)	0.786 (±0.020)	0.9662 (±0.024)
PS-$ZnCl_2$-240-6 h	0.637 (±0.015)	0.653 (±0.015)	1.758 (±0.042)	0.9981 (±0.0236)	0.9481 (±0.0224)	3.035 (±0.072)	0.322 (±0.008)	0.8963 (±0.0212)	0.082 (±0.002)	0.423 (±0.010)	0.9954 (±0.0235)

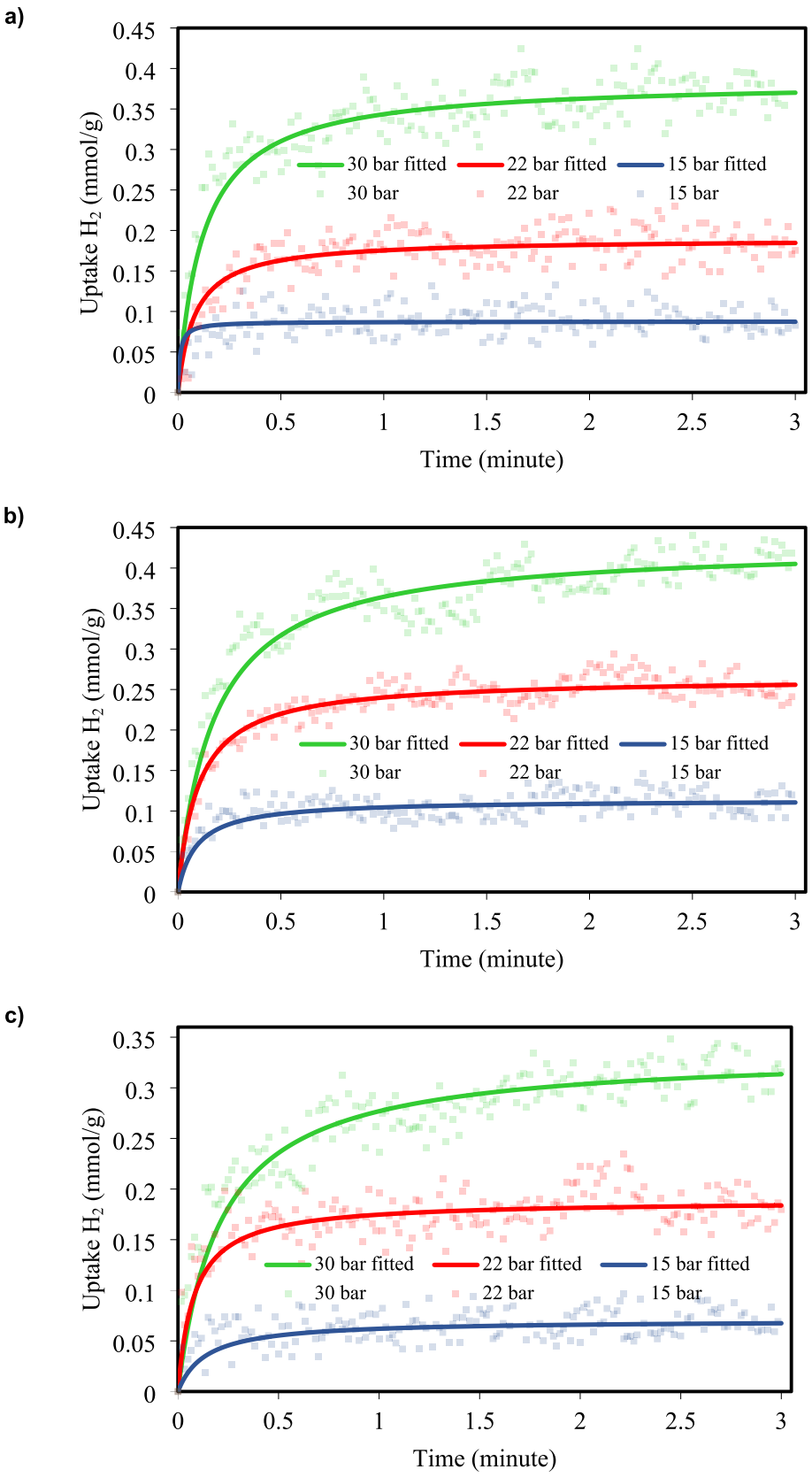

Fig. 8. The changing of the amount of adsorbed hydrogen with time for a) PS-ZnCl2-240-1 h, b) PS-ZnCl2-240-3 h and c) PS-ZnCl2-240-6 h samples at different pressures.

liquid phase to the solid surface. The pseudo-first-order kinetic equation states that the adsorption rate is proportional to the change in the concentration of the adsorbate. The pseudo-first-order equation can be written in linear form as follows:

$$\ln(q_e - q_t) = \ln q_e - k_1 t \quad (5)$$

In this equation, q_e is the amount of adsorbate adsorbed at equilibrium (mmol/g); q_t is the amount of adsorbate adsorbed at any time t (mmol/g); t is time (min); and k_1 is the rate constant (min^{-1}). For the experimental data to be compatible with this equation, the plot of $\ln(q_e - q_t)$ against t should give a straight line with slope $-k_1$ and extrapolation $\ln q_e$.

The pseudo-second order kinetic equation states that the reaction rate is proportional to the square of the adsorbate concentration. According to this model, the kinetic equation in linear form is

$$\frac{t}{q_t} = \frac{1}{k_2 q_e^2} + \frac{t}{q_e} \quad (6)$$

In this equation, k_2 is the rate constant (mmol/g min). If the plot of t/q_t against t gives a straight line, q_e can be calculated from the slope of the line and then k_2 can be calculated from extrapolation.

The regression coefficient values obtained by applying the experimental data to the pseudo first and second order kinetic equations are given in Table 7. The regression coefficient values for the pseudo first order kinetic equation vary in the range of 0.2835–0.6806, while they vary in the range of 0.8680–0.9874 for the second order kinetic equation. These values show that the second order kinetic equation is in good agreement with the experimental data. Another parameter that shows that the experimental data are compatible with this equation is the agreement between the experimental and computational q_e values. The points in Fig. 9 represent the experimental data, while the lines show the fitting curves for the q_e and k_2 values calculated from the pseudo-second order. Fig. 9 shows the curves of t/q_t against t for the activated carbon samples. Similar results are available in the literature. For example, the defective fullerenes were produced from fullerenes by mechanical grinding at different grinding rates and times, and the adsorption kinetics of these structures were investigated with pseudo-first and second-order equations. The kinetic analysis results showed that both the regression coefficients for the pseudo-second-order kinetic equation were higher and the experimental and computational q_e values were in good agreement with each other [81]. In addition, it was determined that the adsorption kinetics of benzene vapors on the surface of biochar produced from almond shells was also compatible with the pseudo-second-order kinetic equation [82]. The adsorption kinetic analysis of hydrogen on the $Pt/TiO_2/Pt$ structure revealed that the experimental data showed high agreement with the pseudo second-order model. This model is used to determine the hydrogen flux and diffusion rate, explaining how hydrogen interacts with the chemicals on the surface [83]. The adsorption kinetics of NO_2 on SnO_2/RGO nanohybrids were investigated using Elovich and pseudo second-order models. Experimental data show that at low NO_2 concentrations (1 ppm), the adsorption obeys the Elovich model. In this case, the response time was measured as 10 s and the return time as 20 s. At higher concentrations (6 and 9 ppm), it was observed that the linear relationship decreased, which revealed that the adsorption kinetics were also supported by the second-order reaction kinetics [84].

In order to interpret experimental data from a mechanistic point of view, it is necessary to define the steps that occur during adsorption. In general, during adsorption, the adsorbate diffuses from the bulk phase to the solid surface, the adsorbate diffuses intraparticle in the internal pores of the adsorbent, and the adsorbate adsorbs on the active sites on the adsorbent surface. In general, the adsorption of the adsorbate on the active sites on the adsorbent surface occurs very quickly and this step does not constitute the rate-determining step [85]. Therefore, the experimental data can be analyzed with the Boyd and Weber-Morris

Table 7
Calculated kinetic constants for the adsorption of hydrogen on activated carbon samples.

Samples	Pressures (bar)	Pseudo-first order	Pseudo-second order				Boyd R^2	Weber-Morris			
		R^2	R^2	$q_{e(exp)}$ (mmol/g)	$q_{e(cal)}$ (mmol/g)	k_2		R_1^2	k_1	R_2^2	k_2
PS-$ZnCl_2$-240-1 h	30	0.5157 (±0.0112)	0.9810 (±0.0213)	0.424 (±0.009)	0.385 (±0.008)		21.53 (±0.47)	0.4552 (±0.0099)	0.8089 (±0.0176)	0.428 (±0.0093)	0.3769 (±0.0082)	0.0649 (±0.0014)
	22	0.1944 (±0.0042)	0.9482 (±0.0206)	0.229 (±0.005)	0.190 (±0.004)		64.82 (±1.41)	0.2700 (±0.0059)	0.8560 (±0.0186)	0.293 (±0.006)	0.0741 (±0.0016)	0.0179 (±0.0004)
	15	0.0285 (±0.0006)	0.8934 (±0.0194)	0.132 (±0.003)	0.088 (±0.002)	1160 (±25)		0.0509 (±0.0011)	0.6506 (±0.0141)	0.149 (±0.003)	0.0001 (±0.000002)	0.0004 (±0.000009)
PS-$ZnCl_2$-240-3 h	30	0.5772 (±0.0143)	0.9874 (±0.0245)	0.440 (±0.011)	0.429 (±0.011)		13.18 (±0.33)	0.5561 (±0.0138)	0.9454 (±0.0234)	0.522 (±0.013)	0.6035 (±0.0150)	0.084 (±0.002)
	22	0.4621 (±0.0115)	0.9857 (±0.0244)	0.294 (±0.007)	0.264 (±0.007)		37.43 (±0.93)	0.4318 (±0.0107)	0.9409 (±0.0233)	0.362 (±0.009)	0.3855 (±0.0096)	0.038 (±0.001)
	15	0.1422 (±0.0035)	0.9363 (±0.0232)	0.136 (±0.003)	0.114 (±0.003)		97.44 (±2.42)	0.2292 (±0.0057)	0.8126 (±0.0202)	0.157 (±0.004)	0.1005 (±0.0025)	0.014 (±0.0003)
PS-$ZnCl_2$-240-6 h	30	0.6806 (±0.0161)	0.9822 (±0.0232)	0.348 (±0.008)	0.335 (±0.008)		14.06 (±0.33)	0.6479 (±0.0153)	0.8601 (±0.0203)	0.301 (±0.007)	0.6272 (±0.0148)	0.084 (±0.002)
	22	0.2662 (±0.0063)	0.9636 (±0.0227)	0.234 (±0.006)	0.189 (±0.005)		66.09 (±1.56)	0.2770 (±0.0054)	0.7224 (±0.0170)	0.246 (±0.006)	0.1632 (±0.0039)	0.024 (±0.001)
	15	0.1256 (±0.0030)	0.8680 (±0.0205)	0.094 (±0.002)	0.071 (±0.002)		103.2 (±2.4)	0.1461 (±0.0034)	0.4338 (±0.0102)	0.081 (±0.002)	0.0828 (±0.0020)	0.012 (±0.0003)

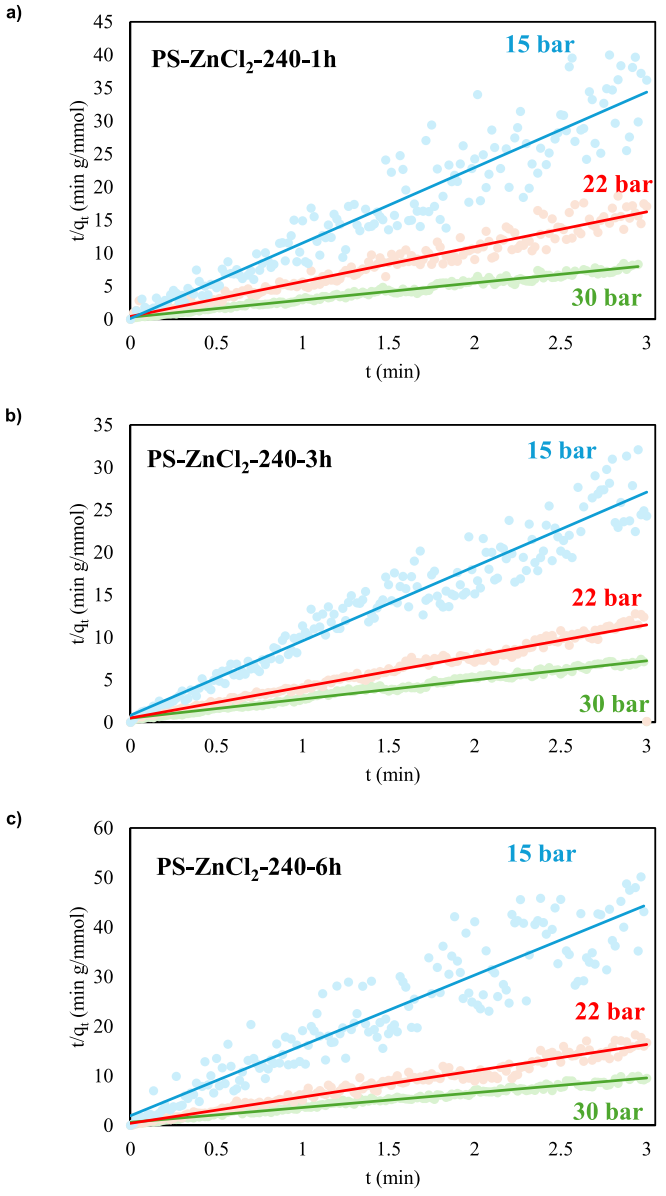

Fig. 9. The curves of t/q_t versus t for samples a) PS-ZnCl2-240-1 h, b) PS-ZnCl2-240-3 h and c) PS-ZnCl2-240-6 h at different pressures.

equations to determine which of the other two steps is the slowest and the rate-determining step.

The diffusion model is based on the Fickian diffusion model, and the Boyd equation for the diffusion of adsorbate from the bulk phase to the solid surface in the adsorption process where solid diffusion dominates can be written as follows [86].

$$\ln\left(1-\frac{q_t}{q_e}\right) = -0.497 - \frac{\pi^2 D_c}{r_c^2} t \tag{7}$$

Here, D_c is the diffusion coefficient (cm^2/min); r_c is the diameter of the adsorbent (cm); t is the time (min); q_t is the amount of adsorbate adsorbed at any time t (mmol/g); and q_e is the amount of adsorbate adsorbed at equilibrium (mmol/g). According to this equation, if the curve of $\ln(1 - q_t/q_e)$ against t gives a straight line passing through the origin, the adsorption mechanism is governed by intraparticle diffusion. If it intersects the y-axis at −0.497, it shows that the adsorption mechanism is governed by external mass transfer.

The Weber-Morris equation is a linear representation used to analyze intraparticle diffusion in adsorption kinetics. According to the Weber-Morris equation, if intraparticle diffusion is the only rate-determining step, the plot of the adsorbed amount versus the square root of time should give a straight line through the origin. If the curve does not pass through the origin, the adsorption process can be represented by multilinear curves representing the different steps. The Weber-Morris equation can be given as follows.

$$q_t = k_{int}\sqrt{t} + C \tag{8}$$

In this equation, k_{int} is the intraparticle diffusion rate constant, and C is a constant that represents the intraparticle diffusion constant.

The regression coefficient values obtained by applying the experimental data to the Boyd and Weber-Morris equations are given in Table 7. The regression coefficient values for the Boyd equation vary in the range of 0.0509–0.6479. The very low regression coefficient values indicate that the adsorption mechanism is not external mass transfer diffusion. Fig. 10 shows the Weber-Morris curves for the experimental data. It is seen from the figures that the curves do not pass through the origin. This situation shows that intraparticle diffusion is not the only

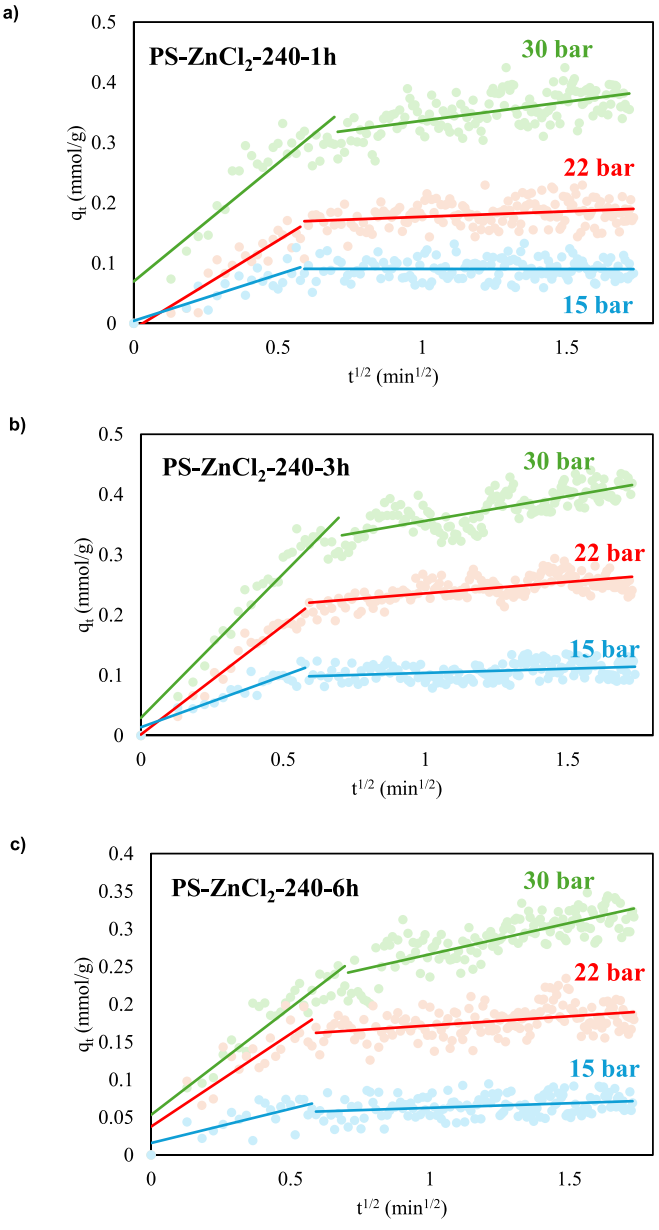

Fig. 10. The curves of q_t versus $t_{0.5}$ for samples a) PS-$ZnCl_2$-240-1 h, b) PS-$ZnCl_2$-240-3 h and c) PS-ZnCl2-240-6 h.

rate-controlling step. Because the figures exhibit two intersecting curved lines. The regression coefficient values calculated for the Weber-Morris curves are shown in Table 7. It is seen that the regression coefficient values for the first region are in the range of 0.4338–0.9454 and the regression coefficient values for the second region are very low. In addition, at low pressures, the extensions of the Weber-Morris curves pass through points very close to the origin. The fact that the experimental data are not compatible with the Boyd equation, the fact that the Weber-Morris curves pass through points very close to the origin at low pressures and the regression coefficient of the first region is higher reveals that the rate-determining step in the adsorption process is the intraparticle diffusion step. The adsorption kinetics of methylene blue on the hazelnut shell was investigated. The experimental results showed that the adsorption provided good agreement with the pseudo-second-order kinetic model (R^2 value in the range of 0.9991–0.9999). In addition, the intraparticle diffusion process was determined as the rate-determining step in the adsorption process [87]. In another study, the adsorption kinetics of maxilon blue GRL on sepiolite was investigated. Experimental data show that the kinetic behavior of adsorption can be best described by the pseudo-second-order model. Furthermore, the intra-particle diffusion process has been identified as the rate-limiting step of the adsorption process [85].

3.5. Conclusions

In this study, the cryogenic hydrogen storage performance of activated carbons synthesized from a low-cost and sustainable biomass source—peanut shells—was comprehensively investigated. Activated carbons were produced via hydrothermal carbonization, with chemical activation using $ZnCl_2$. The process yielded significant enhancements in surface area and pore structure. Among the prepared samples, the PS-$ZnCl_2$-240-3 h material exhibited the highest BET surface area (856 m^2/g) and total pore volume (0.448 cm^3/g), achieving a maximum hydrogen uptake of 2.1 wt% at 77 K and 30 bar. This performance is competitive compared to similar biomass-derived carbons reported in the literature under equivalent conditions.

Comprehensive characterization analyses revealed the structural and morphological evolution of the carbon materials. FTIR-ATR spectra confirmed the elimination of oxygen-containing functional groups during activation, indicating an increase in carbonization content. XRD patterns showed the amorphous nature of the $ZnCl_2$-activated samples, while SEM images displayed the progressive development of porosity with increasing activation time. The PS-$ZnCl_2$-240-3 h sample demonstrated a well-balanced micro- and mesoporous structure, supported by DFT analysis, which quantified the micropore volume as 0.346 cm^3/g and mesopore volume as 0.102 cm^3/g. EDX results indicated a substantial increase in carbon content (up to 88.14 %) and a decrease in oxygen content, highlighting a favorable surface composition for hydrogen adsorption. Furthermore, TGA analyses demonstrated enhanced thermal stability in the activated carbons, particularly for the 3 h and 6 h activation times.

Adsorption isotherm modeling showed that all samples followed the Langmuir model with high correlation coefficients ($R^2 > 0.996$), suggesting monolayer physisorption behavior. Kinetic analyses demonstrated that the hydrogen adsorption process was best described by the pseudo-second-order model, while Boyd and Weber–Morris models indicated that intraparticle diffusion was the rate-limiting step. The PS-$ZnCl_2$-240-3 h sample, in particular, exhibited fast adsorption kinetics and the highest agreement with theoretical models.

In addition to material performance, the study offers important implications from a process engineering perspective. The hydrothermal carbonization process, conducted at a relatively low temperature (240 °C) and moderate reaction times (1–6 h), is energy-efficient and environmentally benign. The use of $ZnCl_2$ as an activating agent enables high porosity formation in a short period, while minimizing chemical consumption and secondary waste generation. The simplicity and reproducibility of the synthesis steps—combined with standard equipment such as a stainless-steel autoclave and vacuum filtration—enhance the scalability of the process from laboratory to pilot scale.

In conclusion, activated carbons derived from peanut shells present not only excellent structural and adsorption properties but also offer a promising, sustainable, and process-efficient route for cryogenic hydrogen storage applications. With optimized pore structures and favorable kinetics, these materials hold strong potential for integration into future energy storage systems.

CRediT authorship contribution statement

Yasemin Turhan: Writing – review & editing, Writing – original draft, Visualization, Validation, Supervision, Software, Resources, Project administration, Methodology, Investigation, Funding acquisition, Formal analysis, Data curation, Conceptualization. **Merve Boyluca Yeşilbiçer:** Software, Methodology, Investigation, Formal analysis, Data curation. **Berna Koçer Kizilduman:** Writing – original draft, Methodology, Investigation. **Mehmet Doğan:** Writing – original draft, Methodology, Investigation. **Zeynep Bicil:** Writing – original draft, Software, Methodology, Investigation, Data curation.

Ethical approval

No experiments were conducted in this study that required ethical approval.

Funding

This project received funding from the Scientific Research Projects Commission of Balikesir University (Project Number: BAP 2017/084).

Declaration of competing interest

The authors declare the following financial interests/personal relationships which may be considered as potential competing interests: Yasemin Turhan reports financial support was provided by Balikesir University — Cagis Campus. If there are other authors, they declare that they have no known competing financial interests or personal relationships that could have appeared to influence the work reported in this paper.

Data availability

The authors do not have permission to share data.

References

[1] G.L. Kyriakopoulos, K.G. Aravossis, Literature review of hydrogen energy systems and renewable energy sources, Energies 16 (22) (2023) 7493.
[2] J. Gómez, R. Castro, Green hydrogen energy systems: a review on their contribution to a renewable energy system, Energies 17 (13) (2024) 1–41.
[3] M. Sevilla, R. Mokaya, Energy storage applications of activated carbons: supercapacitors and hydrogen storage, Energy Environ. Sci. 7 (4) (2014) 1250–1280.
[4] G. Sethia, A. Sayari, Activated carbon with optimum pore size distribution for hydrogen storage, Carbon 99 (2016) 289–294.
[5] M. Jordá-Beneyto, F. Suárez-García, D. Lozano-Castelló, D. Cazorla-Amorós, A. Linares-Solano, Hydrogen storage on chemically activated carbons and carbon nanomaterials at high pressures, Carbon 45 (2) (2007) 293–303.
[6] R.C. Lochan, M. Head-Gordon, Computational studies of molecular hydrogen binding affinities: the role of dispersion forces, electrostatics, and orbital interactions, Phys. Chem. Chem. Phys. 8 (12) (2006) 1357–1370.
[7] E. Klontzas, E. Tylianakis, G.E. Froudakis, On the enhancement of molecular hydrogen interactions in nanoporous solids for improved hydrogen storage, J. Phys. Chem. Lett. 2 (2011) 1824–1830.
[8] M. Kalibek, A. Ospanova, B. Suleimenova, R. Soltan, T. Orazbek, A. Makhmet, Kh. S. Rafikova, N. Nuraje, Solid-state hydrogen storage materials, Discov. Nano 19 (1) (2024).

[9] D. Lozano-Castelló, F. Suárez-García, Á. Linares-Solano, D. Cazorla-Amorós, Advances in hydrogen storage in carbon materials, Renew. Hydr. Technol. (2013) 269–291.

[10] G. Sethia, A. Sayari, Nitrogen-doped carbons: remarkably stable materials for CO_2 capture, Energy Fuel 28 (4) (2014) 2727–2731.

[11] A. Flamina, R.M. Raghavendra, A. Subramaniam, Agarose derived carbon based nanocomposite for hydrogen storage at near-ambient conditions, Carbon 230 (2024) 119657, https://doi.org/10.1016/j.carbon.2024.119657. ISSN 0008-6223.

[12] K. Soni, N.L. Panwar, P.R. Lanjekar, Emergence of carbonaceous material for hydrogen storage: an overview, Clean Energy 8 (4) (2024) 147–168.

[13] R. Pachaiappan, L. Cornejo-Ponce, P.E. Saranya, K. Manavalan, T.K. Nguyen, Chapter 22—Carbon-based micro- and nanomaterials for hydrogen production and storage, in: Nanotechnology for Hydrogen Production and Storage Nanostructured Materials and Interfaces, 2024, pp. 607–633.

[14] Ü. Çakır, F. Kestel, B.K. Kızılduman, Z. Bicil, M. Doğan, Multi walled carbon nanotubes functionalized by hydroxyl and schiff base and their hydrogen storage properties, Diam. Relat. Mater. 120 (2021) 108604.

[15] M. Doğan, A. Selek, O. Turhan, B.K. Kızılduman, Z. Bicil, Different functional groups functionalized hexagonal boron nitride (h-BN) nanoparticles and multi-walled carbon nanotubes (MWCNT) for hydrogen storage, Fuel 303 (2021) 121335.

[16] B.K. Kızılduman, Y. Turhan, M. Doğan, Mesoporous carbon spheres produced by hydrothermal carbonization from rice husk: optimization, characterization and hydrogen storage, Adv. Powder Technol. 32 (2021) 4222–4234.

[17] S.H. Hwang, Y.K. Kim, H.J. Seo, S.M. Jeong, J. Kim, S.K. Lim, The enhanced hydrogen storage capacity of carbon fibers: the effect of hollow porous structure and surface modification, Nanomaterials 11 (7) (2021) 1830.

[18] D. Wei, X. Shi, H. Junge, C. Du, M. Beller, Carbon neutral hydrogen storage and release cycles based on dual-functional roles of formamides, Nat. Commun. 14 (2023) 3726.

[19] E. Biehler, Q. Quach, T.M. Abdel-Fattah, 2-Dimensional and 3-dimensional carbon structures for hydrogen storage, in: ECS Meeting Abstracts, MA2023-02, 2023, p. 1038.

[20] A. Jain, R. Balasubramanian, M.P. Srinivasan, Hydrothermal conversion of biomass waste to activated carbon with high porosity: a review, Chem. Eng. J. 283 (2016) 789–805.

[21] T. Kopac, Hydrogen storage characteristics of bio-based porous carbons of different origin: a comparative review, Int. J. Energy Res. 45 (15) (2021) 20497–20523.

[22] R.F. Susanti, R.G.R. Wiratmadja, H. Kristianto, A.A. Arie, A. Nugroho, Synthesis of high surface area activated carbon derived from cocoa pods husk by hydrothermal carbonization and chemical activation using zinc chloride as activating agent, Mater. Today Proc. 63 (2022) 55–60.

[23] S. Kumar, D. Singh, A. Singh, M. Srivastava, S. Kumar, R. Singh, T. Yadav, M. A. Alheety, Pramod K. Singh, Waste peanut shells derived activated carbon for dual electrochemical applications, Energy Storage 6 (1) (2024) 571.

[24] I. Ozdemir, M. Şahin, R. Orhan, M. Erdem, Preparation and characterization of activated carbon from grape stalk by zinc chloride activation, Fuel Process. Technol. 125 (2014) 200–206.

[25] A.R. Hidayu, N.J.P.E. Muda, Preparation and characterization of impregnated activated carbon from palm kernel shell and coconut shell for CO_2 capture, Proc. Eng. 148 (2016) 106–113.

[26] S. Stock, C.O.W. Trost, M. Seyffertitz, J. Selinger, R.K. Gupta, C. Tampaxis, T. A. Steriotis, C. Rebholz, C. Mitterer, O. Paris, N. Kostoglou, Transforming breakfast bio-waste into hydrogen storage materials, Int. J. Hydrog. Energy 114 (2025) 519–533.

[27] Z. Peng, Y. Xu, W. Luo, C. Wang, L. Ma, Conversion of biomass wastes into activated carbons by chemical activation for hydrogen storage, ChemistrySelect 5 (36) (2020) 11221–11228.

[28] A.R. Selvaraj, N. Kostoglou, R. Rajendiran, I. Cho, C. Rebholz, N.D. Chakravarthi, K. Prabakar, Scalable synthesis of biomass-derived three-dimensional hierarchical porous activated carbons for electrochemical energy storage and hydrogen physisorption, J. Energy Storage 92 (2024) 112085.

[29] S. Stock, N. Kostoglou, J. Selinger, S. Spirk, C. Tampaxis, G. Charalambopoulou, T. Steriotis, C. Rebholz, C. Mitterer, O. Paris, Coffee waste-derived nanoporous carbons for hydrogen storage, ACS Appl. Energy Mater. 5 (9) (2022) 10915–10926.

[30] J. Serafin, B. Dziejarski, C. Solis, P.R. de la Piscina, N. Homs, Medium-pressure hydrogen storage on activated carbon derived from biomass conversion, Fuel 363 (2024) 130975.

[31] X. Li, H. Tian, S. Yan, H. Shi, J. Wu, Y. Sun, Y. Xing, H. Bai, H. Zhang, Micropores enriched ultra-high specific surface area activated carbon derived from waste peanut shells boosting performance of hydrogen storage, Int. J. Hydrog. Energy 50 (2024) 324–336.

[32] E. Arslanoğlu, M.Ş. Eren, H. Arslanoğlu, H. Çiftçi, Fabrication, characterization, and adsorption applications of low-cost hybride activated carbons from peanut shell-vinasse mixtures by one-step pyrolysis, Biomass Convers. Biorefinery (2023) 1–15.

[33] A. Sandeep, A.V. Ravindra, Highly efficient peanut shell activated carbon via hydrothermal carbonization and chemical activation for energy storage applications, Diam. Relat. Mater. 146 (2024) 111158.

[34] Z.Y. Zhong, Q. Yang, X.M. Li, K. Luo, Y. Liu, G.M. Zeng, Preparation of peanut hull-based activated carbon by microwave-induced phosphoric acid activation and its application in Remazol Brilliant Blue R adsorption, Ind. Crop. Prod. 37 (1) (2012) 178–185.

[35] M. Faraji, M. Saidi, Experimental and simulation study of peanut shell-derived activated carbon and syngas production via integrated pyrolysis-gasification technique, Process. Saf. Environ. Prot. 171 (2023) 874–887.

[36] A. Ariharan, B. Viswanathan, Porous activated carbon material derived from sustainable bio-resource of peanut shell for H_2 and CO_2 storage applications, Indian J. Chem. Technol. 25 (2018) 140–149.

[37] S. Taşar, F. Kaya, A. Özer, Biosorption of lead (II) ions from aqueous solution by peanut shells: equilibrium, thermodynamic and kinetic studies, J. Environ. Chem. Eng. 2 (2) (2014) 1018–1026.

[38] A. Turkyilmaz, K. Isinkaralar, M. Dogan, B.K. Kizilduman, Z. Bicil, Production, characterization, and hydrogen storage properties of activated carbon from horse chestnut shell, Sustain. Chem. Pharm. 40 (2024) 101634.

[39] R.F.T. Tiegam, D.R.T. Tchuifon, R. Santagata, P.A.K. Nanssou, S.G. Anagho, I. Ionel, S. Ulgiati, Production of activated carbon from cocoa pods: investigating benefits and environmental impacts through analytical chemistry techniques and life cycle assessment, J. Clean. Prod. 288 (2021) 125464.

[40] N.E. Ikladious, N. Shurky, S.F. El-Kalyoubi, J.N. Asaad, S.H. Mansour, S.Y. Tawfik, R.E. Abou-Zeid, Eco-friendly composites based on peanutshell powder/unsaturated polyester resin, in: Proceedings of the Institution of Mechanical Engineers, Part L, 2017, pp. 1–10.

[41] R. Rajbhandari, L.K. Shrestha, B.P. Pokharel, R.R. Pradhananga, Development of nanoporous structure in carbons by chemical activation with zinc chloride, J. Nanosci. Nanotechnol. 13 (4) (2013) 2613–2623.

[42] M. Wu, Q. Guo, G. Fu, Preparation and characteristics of medicinal activated carbon powders by CO_2 activation of peanut shells, Powder Technol. 247 (2013) 188–196.

[43] S.C. Suhdi, Wang, Fine activated carbon from rubber fruit shell prepared by using $ZnCl_2$ and KOH activation, Appl. Sci. 11 (9) (2021) 3994.

[44] M. Woźniak, I. Ratajczak, D. Wojcieszak, A. Waśkiewicz, K. Szentner, J. Przybył, P. Goliński, Chemical and structural characterization of maize stover fractions in aspect of its possible applications, Materials 14 (6) (2021) 1527.

[45] G. Sawargaonkar, R. Pasumarthi, S. Kale, P. Choudhari, S. Rakesh, S. Mutnuri, M. L. Jat, Valorization of peanut shells through biochar production using slow and fast pyrolysis and its detailed physicochemical characterization, Front. Sustain. 5 (2024) 1417207.

[46] M.A. Perea-Moreno, F. Manzano-Agugliaro, Q. Hernandez-Escobedo, A.J. Perea-Moreno, Peanut shell for energy: properties and its potential to respect the environment, Sustainability 10 (9) (2018) 3254.

[47] Z. Zaitun, A. Halim, Y. Sa'dah, R. Cahyadi, Surface morphology properties of biochar feedstock for soil amendment, IOP Conf. Ser. Earth Environ. Sci. 951 (1) (2022) 012034.

[48] J. Hayashi, T. Horikawa, I. Takeda, K. Muroyama, N.A. Farid, Preparing activated carbon from various nutshells by chemical activation with K_2CO_3, J. Carbon 40 (2002) 2381–2386.

[49] D. Kalderis, S. Bethanis, P. Paraskeva, E. Diamadopoulos, Production of activated carbon from bagasse and rice husk by a single-stage chemical activation method at low retention times, Bioresour. Technol. 99 (2008) 6809–6816.

[50] S.S. Abdullah, M.M. Ahmad, L. Ismail, A. Ramli, S. Yusup, Thermogravimetry study on pyrolysis of various lignocellulosic biomass for potential hydrogen production, Int. J. Chem. Biomol. Eng. 3 (2010) 137–141.

[51] W. Tongpoothorn, M. Sriuttha, Preparation of activated carbon from *Jatropha curcas* fruit shell by simple thermo-chemical activation and characterization of their physico-chemical properties, Chem. Eng. Res. Des. 89 (2011) 335–340.

[52] H.M. Al-swaidan, A. Ahmad, Synthesis and characterization of activated carbon from Saudi Arabian dates tree's fronds wastes, in: 3rd Int. Conf. Chem. Biol. Environ. Eng., IACSIT, Singapore, 2011, pp. 25–31.

[53] M. Carrier, A. Loppinet-Serani, D. Denux, J.M. Lasnier, F. Ham-Pichavant, F. Cansell, C. Aymonier, Thermogravimetric analysis as a new method to determine the lignocellulosic composition of biomass, Biomass Bioenergy 35 (1) (2011) 298–307.

[54] D. Bosch, J.O. Back, D. Gurtner, S. Giberti, A. Hofmann, A. Bockreis, Alternative feedstock for the production of activated carbon with $ZnCl_2$: forestry residue biomass and waste wood, Carbon Resour. Convers. 5 (4) (2022) 299–309.

[55] A.R. Ferdous, S.S. Shah, M.N. Shaikh, H.R. Barai, M.A. Marwat, M. Oyama, M. A. Aziz, Advancements in biomass-derived activated carbon for sustainable hydrogen storage: a comprehensive review, Chemistry 19 (16) (2024) e202300780.

[56] Z.S. Doğan, E.E. Doğan, Z. Bicil, B.K. Kızılduman, The effect of Li-doping and doping methods to hydrogen storage capacities of some carbonaceous materials, Fuel 396 (2025) 135280.

[57] M. Doğan, P. Sabaz, Z. Bïcïl, B.K. Kizilduman, Y. Turhan, Activated carbon synthesis from tangerine peel and its use in hydrogen storage, J. Energy Inst. 93 (6) (2020) 2176–2185.

[58] F.N. Yalçınkaya, M. Doğan, Z. Bicil, B.K. Kizilduman, Effect of functionalization and Li-doping methods to hydrogen storage capacities of MWCNTs, Fuel 372 (2024) 132274.

[59] M. Thommes, K. Kaneko, A.V. Neimark, J.P. Olivier, F. Rodriguez-Reinoso, J. Rouquerol, K.S.W. Sing, Physisorption of gases, with special reference to the evaluation of surface area and pore size distribution (IUPAC Technical Report), Pure Appl. Chem. 87 (2015) 1051–1069.

[60] E.E. Doğan, P. Tokcan, B.K. Kizilduman, Storage of hydrogen in activated carbons and carbon nanotubes, Adv. Mater. Sci. 18 (2018) 58.

[61] Y.K. Choi, S.J. Park, Hydrogen storage capacity of highly porous carbons synthesized from biomass-derived aerogels, Carbon Lett. 16 (2015) 127–131.

[62] M.A. de la Casa-Lillo, F. Lamari-Darkrim, D. Cazorla-Amorós, A. LinaresSolano, Hydrogen storage in activated carbons and activated carbon fibers, J. Phys. Chem. B 106 (42) (2002) 10930–10934.

[63] Z. Bicil, M. Dogan, Characterization of activated carbons prepared from almond shells and their hydrogen storage properties, Energy Fuel 35 (12) (2021) 10227–10240.
[64] Y.J. Heo, S.J. Park, Synthesis of activated carbon derived from rice husks for improving hydrogen storage capacity, J. Ind. Eng. Chem. 31 (2015) 330–334.
[65] S.H.M. Arshad, N. Ngadi, A.A. Aziz, N.S. Amin, M. Jusoh, S. Wong, Preparation of activated carbon from empty fruit bunch for hydrogen storage, J. Energy Storage 8 (2016) 257–261.
[66] K. Isinkaralar, G. Gullu, A. Turkyilmaz, M. Dogan, O. Turhan, Activated carbon production from horse chestnut shells for hydrogen storage, Int. J. Glob. Warm. 26 (4) (2022) 361–373.
[67] A.J. Lachawiec, G. Qi, R.T. Yang, Hydrogen storage in nanostructured carbons by spillover: bridge-building enhancement, Langmuir 21 (24) (2005) 11418–11424.
[68] M.S. Ng, H.W.B. Teo, A. Chakraborty, Thermodynamic trends for evaluating hydrogen storage density and energy flow on Maxsorb-III, HKUST-1 and UiO-66 (Zr) MOFs, Ther. Sci. Eng. Progr. 50 (2024) 102549.
[69] N.L. Rosi, J. Eckert, M. Eddaoudi, D.T. Vodak, J. Kim, M. O'Keeffe, O.M. Yaghi, Hydrogen storage in microporous metal-organic frameworks, Science 300 (5622) (2003) 1127–1129.
[70] B. Xiao, P.S. Wheatley, X. Zhao, A.J. Fletcher, S. Fox, A.G. Rossi, R.E. Morris, High-capacity hydrogen and nitric oxide adsorption and storage in a metal–organic framework, J. Am. Chem. Soc. 129 (5) (2007) 1203–1209.
[71] P.B. Rallapalli, M.C. Raj, S. Senthilkumar, R.S. Somani, H.C. Bajaj, HF-free synthesis of MIL-101 (Cr) and its hydrogen adsorption studies, Environ. Prog. Sustain. Energy 35 (2) (2016) 461–468.
[72] A. Kazakov, D. Blinov, I. Romanov, D. Dunikov, V. Borzenko, Metal hydride technologies for renewable energy, in: E3S Web of Conferences vol. 114, EDP Sciences, 2019, p. 05005.
[73] K. Iyakutti, V.J. Surya, R. Lavanya, V. Vasu, R. Rajeswarapalanichamy, Y. Kawazoe, Effects of nanostructures on the hydrogen storage properties of MgH2-A first principles study, Comput. Condens. Matter 30 (2022) e00643.
[74] M. Doğan, M. Alkan, A. Türkyilmaz, Y. Özdemir, Kinetics and mechanism of removal of methylene blue by adsorption onto perlite, J. Hazard. Mater. 109 (1–3) (2004) 141–148.
[75] M. Doğan, Y. Özdemir, M. Alkan, Adsorption kinetics and mechanism of cationic methyl violet and methylene blue dyes onto sepiolite, Dyes Pigments 75 (3) (2007) 701–713.
[76] A. Djelloul, N. Boutaleb, A.O. Ezzat, L. Sabantina, O.H. Abd-Elkader, B.D. Alkoudsi, M. Hamadouche, A. Benyoucef, Polyaniline–modified metal oxides adsorbents for the application in the Congo red dye adsorption, Colloids Surf. A Physicochem. Eng. Asp. 703 (2024) 135266.
[77] D.O. Cooney, On the basis for the Freundlich adsorption isotherm, Chem. Eng. Commun. 94 (1990) 27–34.
[78] P.M. Mathias, R. Kumar, J.D. Moyer, J.M. Schork, S.R. Srinivasan, S.R. Auvil, O. Talu, Correlation of multicomponent gas adsorption by the dual-site Langmuir model. Application to nitrogen/oxygen adsorption on 5A-zeolite, Ind. Eng. Chem. Res. 35 (7) (1996) 2477–2483.
[79] C. Yang, Statistical mechanical aspects of adsorption systems obeying the Temkin isotherm, J. Phys. Chem. 97 (1993) 7097–7101.
[80] M. García-Diéguez, D.D. Hibbitts, E. Iglesia, Hydrogen chemisorption isotherms on Pt particles at catalytic temperatures: Langmuir and two-dimensional gas models revisited. J. Phys. Chem. C, 123 (2019) 1020–1032.
[81] M. Doğan, M.Y. Kalafat, B.K. Kizilduman, Z. Bicil, Y. Turhan, E. Yanmaz, B. Duman, Hydrogen storage analysis of fullerene and defective fullerenes: the first experimental study, Fuel 390 (2025) 134705.
[82] S. Kutluay, Gas phase adsorption of benzene volatile organic compound onto char produced from almond shells: kinetics, equilibrium and thermodynamics, BEÜ Fen Bilimleri Derg. 8 (4) (2019) 1432–1445.
[83] A.A. Haidry, Y. Ji, A. Raza, H. Zhu, A. Zavabeti, B. Saruhan, Elucidating the hydrogen adsorption kinetics on Pt/TiO_2/Pt based highly efficient sensors, Mater. Res. Bull. 167 (2023) 112415.
[84] B. Bhangare, N.S. Ramgir, S. Jagtap, A.K. Debnath, K.P. Muthe, C. Terashima, D. K. Aswal, S.W. Gosavi, A. Fujishima, XPS and Kelvin probe studies of SnO_2/RGO nanohybrids based NO_2 sensors, Appl. Surf. Sci. 487 (2019) 918–929.
[85] M. Doğan, M. Alkan, Ö. Demirbaş, Y. Özdemir, C. Özmetin, Adsorption kinetics of maxilon blue GRL onto sepiolite from aqueous solutions, Chem. Eng. J. 124 (2006) 89–101.
[86] K.H. Chu, M.A. Hashim, G. Hayder, Boyd's film diffusion model for water contaminant adsorption: time for an upgrade? J. Mol. Liq. 409 (2024) 125466.
[87] M. Doğan, H. Abak, M. Alkan, Adsorption of methylene blue onto hazelnut shell: kinetics, mechanism and activation parameters, J. Hazard. Mater. 164 (2009) 172–181.